Word count: 6284 Revision 1

Experimental partitioning of fluorine and barium in lamproites

Isra S. Ezad[1] and Stephen F. Foley[1]

[1]Department of Earth and Environmental Sciences, Macquarie University, Balaclava Road, North Ryde, Sydney, NSW, 2109, Australia
isra.ezad@mq.edu.au

Abstract

The dynamic properties and melting behaviour of the Earth's mantle are strongly influenced by the presence of volatile species including water, carbon dioxide and the halogens. The role that halogens play in the mantle has not yet been fully quantified: their presence in only small quantities has dramatic effects on the stability of mantle minerals, melting temperatures and in generating halogen-rich melts such as lamproites. Lamproites are volumetrically small volcanic deposits but are found on every continent on the planet: they are thought to be melts generated from volatile-rich mantle sources rich in fluorine and water. To clarify the mantle sources of lamproites we present experimentally determined mineral/melt partition coefficients for fluorine and barium between phlogopite and lamproite melts. Both fluorine and barium are compatible in phlogopite ($D_F^{(Phl/Melt)} 0.96 \pm 0.02 - 3.44 \pm 0.33, D_{Ba}^{(Phl/Melt)} 0.52 \pm 0.05 - 3.68 \pm 0.43$) at a range of pressures (5 – 30 kbar), temperatures (1000 - 1200°C), and fluid compositions (C-O-H mixtures). Using our partition coefficients, we model the melt compositions produced by potential lamproite sources, including phlogopite garnet lherzolite, phlogopite harzburgite, and hydrous pyroxenite. The results demonstrate that hydrous pyroxenites and phlogopite garnet lherzolite can produce melts with F and Ba contents similar to lamproites, but only hydrous pyroxenites fully reproduce other geochemical characteristics of lamproites including high K_2O, low CaO content, and high F/H_2O ratios.

Introduction

The Earth's mantle is a reservoir for highly incompatible and volatile elements including hydrogen, carbon, halogens, and barium (Bell and Rossman, 1992; Karato, 2011; Klemme and Stalder, 2018; Koga and Rose-Koga, 2018). The role and importance of H_2O and CO_2 in the mantle has been of interest for many decades, with direct observations supplied by investigations of mantle xenoliths (e.g. Carswell and Dawson, 1970; Dawson, 1971; Richardson et al., 1985; Safonov et al., 2019; Tollan et al., 2015; Waters, 1987). More recently extensive experimental studies have explored the role and effects of H_2O and CO_2 in the mantle and during melting (Dasgupta et al., 2013; Dasgupta and Hirschmann, 2010, 2006; Foley et al., 2009; Green, 2015, 1990; Green et al., 2014, 2010; Kovács et al., 2012; Pintér et al., 2021). Despite the growing interest in volatile elements, halogens have received less attention even though their presence in small concentrations has profound effects on solidus temperatures (Brey et al., 2009), the stability of minerals (Foley, 1991) and potential deep mantle storage of halogens (Grützner et al., 2017; Roberge et al., 2015).

The common halogens (F, Cl, I, & Br) and barium are considered to be moderately to highly incompatible in most anhydrous silicate minerals (Fabbrizio et al., 2013; Joachim et al., 2017), whereas F is compatible in apatite, phlogopite, amphibole and titanates (Chevychelov et al., 2008; Edgar and Arima, 1985; Edgar and Charbonneau, 1991; Edgar and Pizzolato, 1995; Flemetakis et al., 2021; Li et al., 2018; Vukadinovic and Edgar, 1993). All of these may occur as accessory minerals in mantle peridotites (Grégoire et al., 2002; Kelley, 2000) and as more common minerals in some pyroxenites (Fitzpayne et al., 2018a; Sweeney et al., 1993; Waters, 1987). These halogen-bearing minerals are the principal reservoirs of fluorine in the upper mantle, and apatite and phlogopite may additionally accommodate several

weight percent of barium in their structures (Shaw and Penczak, 1996; Solovova et al., 2009; Wendlandt, 1977).

Fluorine concentrations in continental mantle-derived melts are overwhelmingly influenced by the halogen-bearing minerals, and it has been demonstrated that F content increases with increasing melt alkalinity (Edgar et al., 1996), with ultrapotassic melts considered to have the highest F contents of known primary mantle melts (Edgar et al., 1996; Foley et al., 1987).

The causes of F and Ba enrichments in lamproites have been the subject of many scientific studies but have proven challenging to identify (Edgar et al., 1996, 1992; Edgar and Vukadinovic, 1993; Foley, 1992, 1993, 1990a, 1990b, 1989a, 1989b; Foley et al., 1987, 1986; Fritschle et al., 2013; Mitchell, 2021, 1995; Mitchell and Bergman, 1991; Murphy et al., 2002; Tappe et al., 2008; Vukadinovic and Edgar, 1993). Whilst a complete consensus on the source of lamproites has not been reached there is some agreement that phlogopite, amphibole, apatite and titanates are likely to play important roles in generating parental melts of lamproites (Edgar and Pizzolato, 1995; Edgar and Vukadinovic, 1993; Fitzpayne et al., 2018a; Foley, 1992; Konzett et al., 1997; Mitchell, 1995; Sweeney et al., 1993; Tappe et al., 2008; Vukadinovic and Edgar, 1993). Of these minerals, phlogopite is often present as a phenocryst phase in lamproites and the coupled behaviour of F vs. K_2O attests to the presence of phlogopite in the source of lamproite melts (Aoki et al., 1981; Edgar and Charbonneau, 1991; Mitchell, 2021). Lamproites are highly enriched in incompatible elements including Rb, Sr, Ba, light rare-earth elements (LREE), Zr, Nb, Pb, Th and U. Of these elements, concentrations of barium are extremely high, in some cases up to 1.7 wt% (Guo and Green, 1990; Jaques et al., 1986, 1984). The enrichments in BaO appear to be common to all lamproites (Jaques et al., 1986; Murphy et al., 2002; Sheppard and Taylor, 2019; Solovova et al., 2009; Wendlandt, 1977), and with few common mantle minerals able to accommodate

appreciable quantities of Ba into their structure, phlogopite and apatite present themselves again as key minerals in the generation of lamproite melts.

To understand the role phlogopite may play in the genesis of lamproite melts, this study experimentally determines F and Ba phlogopite/melt partition coefficients for lamproitic melts over a wide range of pressure, temperature, fO_2 and mixed volatile species. These newly determined partition coefficients are subsequently used to interrogate possible mantle sources and their F/H_2O ratios with partial melting models for lamproite melts.

Experiments and analytical methods

High pressure experiments

To constrain mineral/melt partition coefficients, high-pressure, high-temperature experiments described in Foley (1989a) were revisited. These liquidus experiments were conducted on two synthetic lamproite compositions (Table 1): (i) an olivine lamproite primary magma composition for West Kimberley, Australia, and (ii) a leucite lamproite based on the Gaussberg lamproite, Antarctica. The starting mixtures consisted of sintered oxides and carbonates, fluorine was added as MgF_2, and experiments were run in C-O-H fluid saturated conditions which buffered water activity and oxygen fugacity; the experimental design is fully described in Foley (1989b) and so briefly summarized here.

All experiments were performed in a ½" piston cylinder apparatus using a talc or NaCl assembly, temperatures were measured with $Pt/Pt_{90}Rh_{10}$ (S-type) thermocouples. Synthetic starting materials were loaded in graphite inner capsules, with an extra graphite inner capsule containing an iron-wüstite buffer to prevent oxidation and iron loss to outer noble metal capsules of Pt or $Ag_{50}Pd_{50}$. C-O-H fluids were produced from a solid source of Al_4C_3 + $Al(OH)_3$, and 12 wt% distilled H_2O was added to sample capsules via microsyringe (Foley, 1989b). This produces a mixture of CH_4 and H_2O at high pressures: it does not buffer oxygen fugacity exactly (Taylor and Foley, 1989) but the extra H_2O added ensures fO_2 close to, but

below the water maximum in most cases. The oxygen fugacity is well characterised by the fluid composition, which was measured after each run by puncturing the capsule at 150˚C in a GCMS (Taylor and Foley, 1989). This also confirmed fluid saturation in all experiments. The range of oxygen fugacities achieved is shown in Figure 1, in which the fO_2 is plotted against fluid composition, simplified as mol% H_2O in the fluid. The position of the graphite saturation curve is shown exemplarily for 20 and 40 kbar and shows a "water maximum" at intermediate fO_2 at which fluids contain >90% H_2O. At lower fO_2, fluids are principally H_2O+CH_4 mixtures, and H_2O+CO_2 mixtures at higher fO_2 than the water maximum. The fluid compositions measured for individual experiments at 20 kbar (Table 2) are superimposed on Figure 1, from which it can be seen that the majority, which have H_2O>CH_4, lie 1-1.5 log units above the iron-wüstite buffer and well within 1 log unit of each other. Two experiments had measured H_2O+CO_2 mixtures, which lie at about 1.5 log units higher fO_2 than those with H_2O+CH_4 mixtures, and very similar fO_2 to each other despite their disparate fluid compositions (Figure 1). The analysed fluid compositions match closely those calculated for the same conditions (Taylor and Foley, 1989), which demonstrates that equilibrium was achieved in the experiments.

In addition, to revisiting old experiments, results for 3 new high-pressure, high-temperature experiments are also presented for natural leucite lamproites from Gaussberg, Antarctica and West Kimberley, Australia. Full results of these experiments will be presented elsewhere, but are used here to provide an excellent comparison between natural and synthetic lamproites.

Starting materials for these new experiments were ground under propanol to an initial 0.5 µm mixture, and 5 or 10 wt% water was added via micro-syringe directly in the platinum capsules and welded shut. Platinum capsules were enriched in iron by heating with wüstite under vacuum for several days to prevent iron loss from the starting materials during experiments. Experiments were performed at Macquarie University using a rapid quench

end-loaded piston cylinder apparatus with a ½"assembly of natural CaF_2. Temperature was monitored with Type B $Pt_{30}Rh_{70}$ – Pt_6Rh_{94} thermocouples and pressure calibrations were conducted using the quartz-coesite transition (Perrillat et al., 2003) and the albite = jadeite+quartz reaction (Holland, 1980). Experimental charges were first brought to the desired pressure before being rapidly heated at 41°C per minute to above liquidus conditions, and slowly cooled at a rate of 10°C per minute until the final run temperature was achieved (Table 2). Run durations lasted 15 - 24 hours to ensure the growth of large primary phlogopite, experiments were rapidly quenched by switching off power to the furnace and room temperature was reached in 10 seconds. Details of all experiments and run products are provided in Table 2.

Analytical methods

Samples were recovered from high-pressure, high-temperature experiments following decompression and sliced into three discs by diamond wire saw before embedding into epoxy resin. Mounts were polished to a 3 μm diamond finish to ensure accurate chemical compositions could be determined (Figures 2 & 3).

Compositions of phlogopite and quenched glasses were quantified using wavelength-dispersive spectroscopy (WDS) at the Australian National University using a 5 spectrometer Field Emission Electron Probe Analyser (FE-EMPA) JEOL JXA 8530F, operating at 15 kV and 20 nA. WDS measurements were taken by pre-programming positions for phlogopite and glass with a minimum of 5 analyses per mineral/melt pair and running overnight analyses to collect spectra. Two setups were used with different beam current and spot size to ensure volatile components and delicate silicate glasses were not lost or damaged by the electron beam. The first setup was used for collecting mineral chemistry of phlogopite and other silicate phases with a 20 nA beam current, 5-10 μm defocused beam and acquisition to

background time of 90/45s respectively. The second setup was designed to minimise beam damage to quenched glasses, which are feathery in appearance and dominated by clumped patches of phlogopite with other minor phases (Figure 2). Determining compositions of the quench patches required a careful approach to FE-EMPA analysis; spot sizes were increased to a defocused spot of 10-20 μm, where possible, to homogenise the compositions of quenched mats and the beam current was lowered to 3 nA; a minimum of 5 analyses per experimental charge were recorded. In regions free of large primary phlogopite, grid analyses of 30 points covering approximately a 25 μm area were also taken to assess glass homogeneity.

To ensure high precision and accuracy in the measurements of F and Ba, F was independently assigned to an LTAP spectrometer with peak to background times of 90 and 45 seconds respectively. Fluorine was calibrated against a well-characterised CaF_2 at operating conditions of 15 kV and 20 nA, secondary standards of VG-2 were used to confirm detection limits of 100 ppm (Supplementary Table 1). Barium was calibrated against barite and assigned to LLIF, with the same peak to background times and operating conditions as were used for the collection of fluorine measurements. Mineral and melt compositions are reported in Tables 3 and 4.

High-resolution images of the quenched run products were taken at Macquarie University using an FEI – Field Emission Scanning Electron Microscope (FE-SEM) operating at 15 kV, 11 nA beam current, calibrated to specimen current of 13 nA using a Faraday cup on the sample stage, with a spot size of 14.8 μm and a working distance of ~10 mm.

Results

Experimental run products are reported in Table 2 and Figures 2 - 3, mineral compositions in Table 3 and Figure 4, melt compositions in Table 4, and partition coefficients in Table 5 and

Figure 5. Mineral compositions of accessory phases, olivine and clinopyroxene are reported in Supplementary Table 2.

Phlogopite

Large 50 – 200 μm primary phlogopite is present in all experiments, with secondary silicate phases including olivine, clinopyroxene and orthopyroxene (Tables 2 & 3, Figures 2 & 3). Phlogopites are inclusion free and recognisable in SEM micrographs as either basal sections or large tabular plates. They are surrounded by matted quench products of phlogopite, spinel, rutile, orthopyroxene, olivine or clinopyroxene, the proportion of each dependent on the experimental pressure Figures 1 & 2 (Foley, 1990a, 1989b).

Experimental phlogopite compositions are presented in Table 3: their compositions are discussed in detail in Foley (1990a, 1989a) but the major element behaviour in phlogopite is reappraised here in view of the improved quantification of major elements and in particular fluorine by FE-EMPA, resulting in small but significant changes to the interpretation of major element behaviour with respect to pressure and temperature (Edgar and Arima, 1985; Foley, 1990a).

Phlogopite in both olivine and leucite lamproite experiments have Al_2O_3 ranging from 13 – 17 wt % and FeO from 3 – 7 wt %. TiO_2 ranges from 1 – 2.5 wt % in the olivine lamproite series and 1.8 – 5 wt % in leucite lamproite phlogopite. The experimental phlogopite compositions are similar to those in natural lamproites, with West Kimberley phlogopite compositions in the range of 8-12 wt % Al_2O_3, 3.5 – 4 wt % FeO, and TiO_2 ranging from 5–6 wt % (Jaques et al., 1986, 1984). Experimental phlogopite compositions produced from the natural West Kimberley and Gaussberg lamproite compositions are also reported in Table 3, for comparison to their synthetic counterparts.

F contents in phlogopites from olivine lamproite experiments range from 0.39 – 0.71 wt % and 0.19 – 0.56 wt % in the leucite lamproites, reflecting the initially higher F content of the

olivine lamproite starting material (Figure 4 a and b). Fluorine contents of natural West Kimberley lamproites are slightly higher at 1 – 2 wt %, possibly reflecting higher source fluorine content.

BaO is also higher in olivine lamproite phlogopites at 1.70 – 3.18 wt % compared to 0.26 – 1.02 wt % in leucite lamproites (Figure 4 c and d). F decreases with increasing pressure across the temperatures investigated here (Figure 4). There is little to no noticeable temperature dependency on either the F or Ba content of the experimental phlogopites (Figure 4 b, d; Foley, 1990a).

The temperature and pressure effects are weak in comparison to the effects of water activity in experimental charges (Foley, 1989a). Olivine lamproite experiments were performed under low oxygen fugacity conditions of approximately IW + 1 to + 1.5 log units fO_2, and varying water activity (X_{H2O}). Most of the olivine lamproites had high water activity with $H_2O > CH_4$ (see Table 1), except for run 1832, which had $H_2O < CH_4$.

Run 1835 ($H_2O>CH_4$) and run 1832 ($H_2O<CH_4$) were both conducted at 20 kbar and 1050°C, with only fluid composition (and so water activity) differing between them. F uptake in phlogopite increased from 0.48 to 0.64 wt % whilst BaO decreased from 3.18 to 2.46 wt % with decreasing water activity, demonstrating the large impact of water activity on phlogopite compositions (Figure 4 a, c) (Foley, 1990a, 1989a).

A similar comparison is more challenging to ascertain in the leucite lamproite series, as all experiments except for run 1951 were conducted at fluid compositions with $H_2O>CH_4$ and there are no other experiments at the same pressure and temperature conditions as run 1951 to draw comparisons from. Run 1951 has the highest F content amongst the leucite lamproite phlogopites, but whether this is controlled by water activity or its low-pressure temperature conditions (5 kbar, 1050°C) cannot be easily distinguished from the current dataset.

Whilst all precautions were taken to ensure only primary phlogopites were analysed, occasional quench phlogopites were identified and differ in chemistry, with higher TiO_2 and SiO_2 contents and lower K_2O and F (Foley, 1990a). These spurious analyses were removed when determining partition coefficients.

Melt

The experiments presented here were conducted at near liquidus conditions to ensure growth of large primary phlogopite and minimise the growth of other silicate phases, and as a result large areas of quenched melt alongside large primary phlogopite were present in all experimental charges (Figures 2-3).

Melt regions consist of quench crystals, phlogopite, olivine, occasional pyroxene, rutile and spinel and have a complex matted to feathery appearance with very few areas of "clean" glass (Figure 1). FE-EMPA measurements were adjusted to homogenise areas of quench crystal growth (see details in analytical methods) and measurements were subsequently compared to those from new experiments run in the rapid quench piston cylinder, which has vastly improved the quench rate, texture and so the homogeneity of glasses (Figure 3). The compositions of melts from Run MO21-061 (Table 4) a West Kimberley leucite lamproite, are similar, within analytical uncertainty, to those in the synthetic leucite lamproite series, providing confidence in the EMPA technique used to homogenise and determine chemical compositions of the melts.

The melts have a restricted range of compositions with SiO_2 varying from 31.3 – 35.6 wt% and 39.5 – 51.8 wt%, K_2O ranges from 1- 5 wt% and 5.4-8.8 wt% in the olivine and leucite lamproite series experiments respectively. Both sets of experimental melt compositions have high K_2O/Na_2O ratios: 2.4-10.65 for the leucite lamproite, 2.2 – 20.67 for the olivine lamproite and a range of 4.7 – 7.7 for the natural West Kimberley and Gaussberg experiments, whilst P_2O_5 content ranged from 0.76 – 2.79 wt%. CaO content is low,

generally below 5.2 wt% reflecting primary compositions of West Kimberley olivine lamproites (average 5.4 wt%) (Jaques et al., 1986) and Gaussberg leucite lamproites (average 4.4 wt%) (Murphy et al., 2002). Run 1835 has the highest CaO content (8.47 wt%), but still falls within the reported range for olivine lamproites (Jaques et al., 1986).

Partition coefficients of fluorine and barium

Partition coefficients $D_F^{(Phl/Melt)}$, $D_{Ba}^{(Phl/Melt)}$ are presented in Table 5 and Figure 5. Fluorine and barium behave compatibly in phlogopite with partition coefficients above 1, with $D_F^{(Phl/Melt)}$ ranging from 0.96 ± 0.02 to 3.44 ± 0.33 and $D_{Ba}^{(Phl/Melt)}$ 0.99 ± 0.11 to 3.68 ± 0.43 across the pressure, temperature and fluid composition range investigated here (Figure 5).

Several previous studies have constrained $D_F^{(Phl/Melt)}$ for various compositions, pressures, and temperatures (Edgar and Pizzolato, 1995; Flemetakis et al., 2021; Vukadinovic and Edgar, 1993), with Vukadinovic and Edgar (1993) reporting $D_F^{(Phl/Melt)}$ 1.24 – 2 for a phlogopite – apatite – melt system, and Edgar and Pizzolato (1995) $D_F^{(Phl/Melt)}$ 0.68 – 1.55 for a K-richterite – apatite – phlogopite – melt system. More recently, Flemetakis et al. (2021) determined $D_F^{(Phl/Melt)}$ for a basanitic system, reporting compatible $D_F^{(Phl/Melt)}$ values of 0.93 ± 0.08 – 2.56 ± 0.15. Our newly determined partition coefficients for lamproite melts agree within reported uncertainties with previous work irrespective of composition, pressure, and temperature, highlighting the ubiquitous compatibility of F in phlogopite (Edgar and Pizzolato, 1995; Flemetakis et al., 2021; Vukadinovic and Edgar, 1993).

Despite the importance of Ba in phlogopite, fewer experimental studies have constrained $D_{Ba}^{(Phl/Melt)}$ for lamproite compositions (Fabbrizio et al., 2010; Guo and Green, 1990; Schmidt et al., 1999). Guo and Green (1990), found $D_{Ba}^{(Phl/Melt)} < 1$ in all their experiments,

despite similar starting compositions and run conditions to those presented here (Figure 6). The cause of the differing $D_{Ba}^{(Phl/Melt)}$ values in the study of Guo and Green (1990) to those presented here is unclear, but could be due to the higher fO_2 conditions and the lack of a free fluid phase in the study of Guo and Green (1990), both of which affect $D_{Ba}^{(Phl/Melt)}$ as demonstrated here. However, Fabbrizio et al. (2010) and Schmidt et al.,(1999) conducted partitioning experiments on the same leucite lamproite composition as Guo and Green (1990), with Fabbrizio et al. (2010) reporting $D_{Ba}^{(Phl/Melt)}$ 1.57 ± 0.16 to 3.08 ± 0.20 and Schmidt et al. (1999) $D_{Ba}^{(Phl/Melt)}$ 0.56 ± 0.03 to 1.61 ± 0.10, both of which are in excellent agreement with the results presented here (Figure 6). Fabbrizio et al. (2010) were also unable to isolate the cause of differing partition coefficients between their study and that of Guo and Green (1990). Without further investigation of mineral/melt pairs in ultrapotassic melts, it is not possible to comment further on these differences. Several other experimental studies (Adam and Green, 2006; Green et al., 2000; Latourrette et al., 1995; Sweeney et al., 1995) also report similarly high $D_{Ba}^{(Phl/Melt)}$ >1 for various compositions of melt including, basanite (Adam and Green, 2006; Latourrette et al., 1995), basalt (Green et al., 2000) and carbonatite (Sweeney et al., 1995).

Whilst the behaviour of both F and Ba is coupled to pressure and temperature in a similar manner (Figure 4), their partition coefficients show opposing trends (Figure 5). Olivine lamproite experiments were conducted over a smaller pressure-temperature range than the leucite lamproite series and as a result, temperature-induced effects on the partition coefficients, whilst present in both experimental series, are more subtle in the olivine lamproites and are therefore not discussed further (Figure 5 a and c). $D_F^{(Phl/Melt)}$ in leucite lamproite experiments decreases with increasing pressure from $D_F^{(Phl/LL\ melt)}$ 2.52 at 15 kbar

303 to 1.42 at 30 kbar and 1100°C, whilst $D_{Ba}^{(Phl/LL\ melt)}$ increases from 1.21 at 15 kbar to 3.08 at
304 30 kbar and 1100°C (Figure 5 b and d).
305 Increasing experimental temperature in the leucite lamproite series results in small increases
306 in the partition coefficients across all experimental temperatures for both F and Ba within the
307 experimental conditions investigated here. The temperature effect is much smaller than the
308 pressure effect for both $D_{Ba}^{(Phl/Melt)}$ and $D_{F}^{(Phl/Melt)}$, with an increase of only 0.5 from
309 $D_{F}^{(Phl/LL\ melt)}$ 0.99 at 1000°C to 1.49 at 1150°C and 30 kbar, as compared to a threefold
310 reduction due to pressure from $D_{F}^{(Phl/LL\ melt)}$ 2.95 at 20 kbar to 1.45 at 30 kbar and 1150°C.
311 Independent of pressure-temperature effects, varying fluid composition influences partition
312 coefficients to a greater degree than either pressure or temperature alone. The effect of water
313 activity can only be assessed for the olivine lamproite (Figure 7) series: runs 1832 (1050°C,
314 20 kbar) and 1795 (1200°C, 30 kbar) are strongly influenced by low water activity resulting
315 in high partition coefficients relative to runs at similar pressure-temperature conditions of
316 $D_{F}^{(Phl/OL\ melt)}$ 1.61 and 1.06 respectively (Figure 7).
317

318 **Discussion**

319 **The role of barium in lamproites**

320 BaO is one of the least considered components in lamproites and yet it is frequently reported
321 in extremely high concentrations; BaO in the West Kimberley olivine and leucite lamproites
322 average at 1.20 and 1.10 wt% respectively (Jaques et al., 1986), and similarly high BaO
323 concentrations up to 5970 ppm are reported in Gaussberg leucite lamproites (Sheraton, 1981;
324 Murphy et al., 2002). Whilst orogenic lamproites show modestly lower BaO contents, these
325 are still appreciably high, ranging from an average of 1924 ppm in Western Mediterranean
326 lamproites (Contini et al., 1993; Pérez-Valera et al., 2013), to 2092 ppm for Eastern
327 Mediterranean lamproites (Prelević et al., 2012, 2005).

These enrichments in BaO attest to the presence of either apatite or phlogopite, or both, in the source regions of lamproitic melts (Edgar and Charbonneau, 1991; Guo and Green, 1990; Mitchell, 1995). The strong association of F with K_2O (Edgar and Charbonneau, 1991) seen across F rich lamproites strongly implies phlogopite is a potential BaO source, as there is no correlation of F with P_2O_5 which would indicate a strong role of apatite as the F and BaO reservoir in the lamproite source (Edgar and Charbonneau, 1991). The importance of phlogopite as a BaO source is, however, complicated by the accommodation of BaO into its structure (Guo and Green, 1990; Krausz, 1974; Sheppard and Taylor, 2019). Our experimental partition coefficients demonstrate the compatible nature of BaO in phlogopite (Figure. 5 c, d & 6), but phlogopites are structurally complex and several substitution mechanisms have been proposed to incorporate barium (Guo and Green, 1990; Mitchell, 1981; Sheppard and Taylor, 2019; Wendlandt, 1977).

The substitution mechanism proposed by Guo and Green (1990):

$$2K + 4(Mg, Fe) + 4Si = Ba + 3Ti + 4Al + [\,]_{VI.XII},$$

an extension to Wendlandt's (1977) suggested mechanism, could explain our experimental phlogopites (Figure 8 a). However, the simplest substitution mechanism:

$$2K = Ba + [\,],$$

also defines a clear trend for our phlogopites (Figure 8 b), demonstrating the lack of understanding of barium incorporation into the phlogopite structure. Other substitution mechanisms such as the $3K^+ + 2(Mg, Fe)^{2+}_{VI} + Al^{3+}_{IV} = Ti^{4+}_{VI} + Fe^{3+}_{IV} + (Na^+, Ba^{2+}) + [\,]_{VI}$ proposed by Mitchell (1981) do not appear to be operating in our phlogopites, most likely due to the low oxygen fugacity of the experiments presented here, as oxygen fugacity and melt composition play a role in determining the substitution mechanism (Foley, 1989a). Phlogopites in this study have underfilled octahedral and interlayer cation sites (Table 3), below the ideal values of 6 and 2 respectively, strongly implying a substitution mechanism

for barium involving the generation of site vacancies. The underfilled octahedral sites may indicate that the substitution mechanism of Guo and Green (1990) is dominant in our experimental phlogopites. Whether this mechanism is favoured by the low oxygen fugacity cannot be explored further without additional experiments.

The challenge in discerning which mechanism(s) is dominant is increased by the low number of reported measurements of BaO from lamproitic phlogopite and melts. Greater emphasis on the collection of BaO content in ultrapotassic and other alkaline rocks is required to further our understanding on the role BaO plays in phlogopite and the genesis lamproite melts.

The generation of lamproites

The geochemical characteristics of lamproites including high Mg-number, Ni and Cr content point towards a primary mantle derived melt, which has experienced minimal modification prior to eruption (Foley et al., 1987; Mitchell, 1995). In addition to these geochemical characteristics, which are used to distinguish primary melts of peridotite, lamproites are highly enriched in many incompatible elements including BaO, have high K_2O/Na_2O ratios, extreme potassium enrichments, as well as high F /H_2O ratios (Beyer et al., 2016; Edgar et al., 1992; Edgar and Arima, 1983; Foley et al., 1987; Mitchell, 1995), all of which cannot be easily sourced from the lithospheric mantle without enrichment in melt or fluid components (Foley, 1992; Mitchell, 2021, 1995). This apparent paradox has resulted in a lively multi-decadal debate as to what the mineralogy and composition of lamproite source rocks really are (Beyer et al., 2016; Edgar and Charbonneau, 1991; Foley, 1993, 1990b, 1990a, 1989; Förster et al., 2018; Jaques et al., 1986; Mitchell, 1995; Murphy et al., 2002), with broad agreement on the need for "mantle metasomatism" to deliver enrichments in volatiles,

377 halogens and potassium to these source lithologies (Foley, 1992, 1990b, 1989b; Mitchell,
378 2021, 1995).

379 There are three main source lithologies discussed in the literature for the production of
380 lamproitic melts: "exotic" rocks which do not significantly interact with the surrounding
381 lherzolite mantle, such as (i) phlogopite harzburgites (Foley, 1992; Mitchell, 1995), (ii)
382 variably metasomatismed garnet lherzolite (Condamine et al., 2016; Mitchell, 2021), and (iii)
383 hydrous pyroxenites or glimmerites (Fitzpayne et al., 2018a; Konzett et al., 1997; Waters,
384 1987). In order to constrain the source lithology of lamproites, the extreme K_2O contents
385 have been the primary focus, as it has been demonstrated melts of dry garnet lherzolite
386 cannot provide the K_2O enrichment required for ultrapotassic magmas (Laporte et al., 2014;
387 Novella and Frost, 2014). Therefore, to generate high K_2O magmas all the aforementioned
388 sources of lamproites contain phlogopite, as this is expected to be the main K-bearing
389 hydrous phase in the upper mantle (Condamine et al., 2016; Condamine and Médard, 2014;
390 Edgar and Arima, 1983; Foley, 1989b; Förster et al., 2018; Mitchell, 1995; Safonov et al.,
391 2019; Thibault et al., 1992). In addition to its high K_2O content phlogopite has the potential
392 to hold several weight percent F and BaO within its structure, which would generate melts
393 enriched in F, K_2O, BaO and H_2O upon melting.

394

395 **Partial melting of phlogopite-bearing sources**

396 Using the partition coefficients for fluorine experimentally determined here, partial melting
397 models were constructed to assess the viability of three potential source lithologies in
398 generating F/H_2O ratios consistent with lamproitic melts. Partial melting was modelled using
399 numerical solutions after Stracke et al. (2003) and Zou (1998) for dynamic non-modal
400 melting with small melt increments. F/H_2O ratios in melts were calculated for partial melt
401 fractions of 1, 5, 10, and 15%. The modelled source composition and melting reactions of

Condamine et al. (2016) were used for metasomatized garnet phlogopite lherzolite (Phl – lherz) and phlogopite harzburgite (Phl – harz) assemblages. Melting reactions for a hydrous phlogopite pyroxenite (Phl – pyrox) assemblage of orthopyroxene, phlogopite, K-richterite and garnet, without additional accessory phases were determined from Foley et al. (in prep.). Fluorine and H_2O mineral/melt partition coefficients for the nominally anhydrous and halogen-free minerals, olivine, orthopyroxene, clinopyroxene and garnet were taken from Beyer et al. (2016), Dalou et al. (2012), Flemetakis et al. (2021), and Hauri et al. (2006). Partition coefficients for phlogopite were our newly determined $D_F^{(Phl/Melt)}$ with an average value of 1.66, and $D_{H2O}^{(Phl/Melt)}$ of 0.53 from Hauri et al. (2006). Finally, a value of $D_F^{(Mineral/Melt)}$ 1.36 and $D_{H2O}^{(Mineral/Melt)}$ 0.243 was used for potassium richterite (Foley et al., in prep.; Hauri et al., 2006). Bulk F and H_2O contents for each of the three sources was assumed to be: 0.4 wt% H_2O and 700ppm F for both Phl - lherz and Phl - harz (Condamine et al., 2016), whilst values of 0.5 wt% H_2O and 2500 ppm F for the Phl - pyrox assemblage were assumed following measurements on natural phlogopite pyroxenites (Funk and Luth, 2013; Waters, 1987). Full details of the modelling including mineral modes, reactions and partition coefficients are provided in Supplementary Table 3.

Our partial melting models (Figures 9 & 10) demonstrate that Phl - lherz and Phl - pyrox mantle assemblages generate F/H_2O ratios in the range expected for lamproites (0.1 - 0.56 F/H_2O: Edgar et al., 1992; Edgar and Arima, 1983; Mitchell, 1995). at small partial melt fractions between 1 – 15%. Phlogopite harzburgite sources require exhaustion of the only fluorine bearing mineral, phlogopite, to produce F/H_2O ratios characteristic of lamproites. Despite this exhaustion in phlogopite it initially appears that the partial melting models cannot decide which of the mantle assemblages, if any, uniquely contributes to lamproitic melts. However, further assessment of F content (Figure 10) demonstrates the varying geochemical behaviour of melts generated by the three mantle lithologies.

Melts of the phlogopite harzburgite assemblage have the highest F content even after 1% partial melting: despite the similar mineral compositions to phlogopite garnet lherzolite, the melting reactions differ significantly and the initially high contribution of phlogopite to the phlogopite harzburgite melts results in the highest F content (Condamine et al., 2016). The incongruent growth of olivine and clinopyroxene further increases the F content of the melt with increased degrees of partial melting (Condamine et al., 2016; Condamine and Médard, 2014). After exhaustion of phlogopite as the main contributing mineral to the melt, the F content will begin to decrease through dilution. Phlogopite is exhausted at melt fractions of 10% and to model higher degrees of partial melting a change in reaction and either pressure or temperature is required to continue melting. It appears unlikely that primary melts generated from phlogopite harzburgite alone can produce both the F/H_2O ratios and F contents characteristic of lamproites.

Melts of metasomatised garnet phlogopite lherzolite and hydrous phlogopite pyroxenite fall within the F range expected for lamproites but show opposing trends with increasing degree of partial melting (Figure 10). A melt fraction of at least 10% of garnet lherzolite is required to enrich melts to the required F/H_2O ratios, but F contents may be expected to decrease at higher degrees of partial melting due to dilution following the exhaustion of phlogopite and the subsequent melting of orthopyroxene and garnet. A reduction in F content is not supported by our modelling, as the incongruent growth of olivine and clinopyroxene retains high levels of F in the melt which remain unchanged to even larger melt fractions (Condamine et al., 2016). Whilst melting of Phl - lherz appears to be an attractive solution in terms of F/H_2O and F content for the genesis of lamproite melts, the major element chemistry of garnet lherzolite melts, hydrous and anhydrous, has been rigorously constrained by experiments (Balta et al., 2011; Brey et al., 2009; Condamine et al., 2016; Foley, 1992; Girnis et al., 1995; Green, 2015; Kinzler, 1997; Walter, 1998) and cannot produce the high

452 $K_2O/Na_2O > 2$, low Ca and high $K_2O > 8$ wt% required for parental melts of lamproites
453 (Condamine et al., 2016; Foley, 1992; Foley et al., 1987; Mitchell, 1995).
454 Previous studies have been used to suggest that hydrous, fluorine rich minerals such as
455 phlogopite do not need to play a significant role in generating ultrapotassic volcanism, and
456 that the high F/H_2O ratios may instead be reconciled by multiple episodes (at least 6) of small
457 degree (1-2%) partial melting of an eclogite assemblage with clinopyroxene as the main
458 contributor to melts (Beyer et al., 2016). However, the role of clinopyroxene in generating
459 potassic volcanism is problematic as the dissolution of large volumes of clinopyroxene will
460 also enrich melts in CaO and Na_2O, in contrast to the low Ca and Na_2O content of lamproites
461 (Dasgupta et al., 2006; Edgar and Vukadinovic, 1993; Foley et al., 1987). Eclogite is not
462 considered important here for generating lamproite melts.
463 Hydrous pyroxenites of varying lithology are widespread as ultramafic xenoliths from
464 cratonic areas. These include MARID (Mica-Amphibole-Rutile-Ilmenite-Diopside) and PIC
465 (Phlogopite-Ilmenite-Clinopyroxene) assemblages entrained in kimberlites (Fitzpayne et al.,
466 2018b; Grégoire et al., 2002). The possible contribution of MARID or MARID-like
467 assemblages to lamproitic melts has been the subject of experimental studies elsewhere
468 (Förster et al., 2018; Konzett et al., 1997; Sweeney et al., 1993). Our partial melting models
469 (Figures 9 and 10) additionally demonstrate that melts from a hydrous pyroxenite assemblage
470 with similar minerals to MARID can reproduce both the high bulk F content, and the F/H_2O
471 ratios characteristic of lamproites. Unlike their anhydrous counterparts, of which partial melts
472 chemically resemble ocean island basalts (Lambart et al., 2016, 2013), melts of MARID-like
473 hydrous pyroxenites have low CaO and high K_2O due to the major initial contribution of K-
474 richterite followed by phlogopite to the initial melts (Foley et al., in prep.) and the expansion
475 of the phase field of clinopyroxene in potassic systems (Melzer and Foley, 2000).
476

Implications for lamproite melt generation

Partition coefficients for F and Ba have been experimentally determined for phlogopite/melt pairs in a lamproitic system at various pressures, temperatures, and fluid compositions. Our experimental results demonstrate that both F and Ba are compatible in phlogopite across a wide pressure-temperature range, and that the composition of a mixed fluid (CH_4 or H_2O rich) appears to affect the partition coefficients to a greater degree than either pressure or temperature. CH_4-rich fluids are likely to be important in the source regions of lamproite melts, where high F concentrations may result from low water activity and oxygen fugacity, indicating that important variations in the partitioning of F do not depend on just pressure or temperature.

The experiments also show barium to be compatible in phlogopite, but the behaviour and role of BaO was not considered in our partial melting models at this stage. It requires further exploration and improved reporting of BaO concentrations in phlogopite, matrices and whole rocks. Current data is insufficient to clarify the incorporation mechanism governing Ba uptake. The substitution mechanisms involving barium may also be influenced by oxygen fugacity conditions (Foley, 1989a; Mitchell, 1981): our experiments were conducted under reduced conditions and additional experiments in other conditions are required to investigate this further.

Utilising our newly determined partition coefficients, partial melting of possible mantle sources with varying phlogopite content were investigated to decipher which mantle compositions could produce lamproitic signatures. All three of the potential sources, phlogopite garnet lherzolite, phlogopite harzburgite and hydrous phlogopite pyroxenite can produce F/H_2O ratios in the range expected for lamproites at modest melt fractions of between 5 – 10%. However, only hydrous phlogopite pyroxenite and phlogopite garnet lherzolite can generate melts with both F content and F/H_2O ratios in the range of natural

lamproites. Not only are lamproites enriched in F and H_2O, but they have high concentrations of incompatible elements such as BaO, which must be accounted for in discussions of source mineralogy.

Partial melting models in conjunction with carefully determined partition coefficients are only the first step in determining the source of lamproite melts. There are geochemical differences between cratonic and orogenic lamproites, which have not been discussed as part of this contribution as the lamproitic compositions in our experiments represent only those from cratonic regions. These geochemical differences are, however, probably due to differences in source mineralogy and or interactions between metasomatic melts and peridotite, which may involve different kinds of hydrous pyroxenite. The sources of many orogenic lamproites are believed to be much shallower (60-100km) and to involve subducted sedimentary materials which greatly complicate the palette of possible minerals in their sources (Prelević et al., 2013). SiO_2-rich orogenic lamproites may even be generated without phlogopite in the source (Wang et al., 2017).

The validity of our modelling and clarification of source compositions requires further partial melting experiments on potential hydrous pyroxenite sources. Equally desirable are reaction experiments between the peridotitic mantle and melts of hydrous pyroxenite as the latter are unlikely to traverse the lithospheric mantle in unmodified and unreacted form (Foley, 1992). With increased emphasis on understanding ultramafic rocks other than peridotite in the mantle, the role of metasomatism and accessory phases in the generation of lamproites is becoming clearer and our study now confirms the essential role phlogopite plays in generating F and H_2O rich lamproite melts.

Acknowledgements

We wish to thank Jeff Chen for assistance with EMPA measurements at the Australian National University, Sean Murray for assistance with high resolution SEM mapping at Macquarie University, and Slava Shcheka for running the high-pressure lab at Macquarie University like a well-oiled machine. This manuscript has benefitted from many scientific discussions with Joshua Shea. This work was funded by the ARC Laureate Fellowship FL180100134 awarded to SFF.

References

Adam, J., Green, T., 2006. Trace element partitioning between mica- and amphibole-bearing garnet lherzolite and hydrous basanitic melt: 1. Experimental results and the investigation of controls on partitioning behaviour. Contributions to Mineralogy and Petrology 152, 1–17. https://doi.org/10.1007/s00410-006-0085-4

Aoki, K., Ishiwaka, K., Kanisawa, S., 1981. Contributions to Mineralogy and Petrology Fluorine Geochemistry of Basaltic Rocks from Continental and Oceanic Regions and Petrogenetic Application, Contrib Mineral Petrol.

Balta, J.B., Asimow, P.D., Mosenfelder, J.L., 2011. Hydrous, Low-carbon Melting of Garnet Peridotite. Journal of Petrology 52, 2079–2105. https://doi.org/10.1093/petrology/egr040

Bell, D.R., Rossman, G.R., 1992. Water in Earth's mantle: The role of nominally anhydrous minerals. Science 255, 1391–1397. https://doi.org/10.1126/science.255.5050.1391

Beyer, C., Klemme, S., Grützner, T., Ireland, T.R., Magee, C.W., Frost, D.J., 2016. Fluorine partitioning between eclogitic garnet, clinopyroxene, and melt at upper mantle conditions. Chemical Geology 437, 88–97. https://doi.org/10.1016/j.chemgeo.2016.05.032

Brey, G.P., Bulatov, V.K., Girnis, A. v., 2009. Influence of water and fluorine on melting of carbonated peridotite at 6 and 10 GPa. Lithos 112S, 249–259. https://doi.org/10.1016/j.lithos.2009.04.037

Carswell, D.A., Dawson, J.B., 1970. Garnet peridotite xenoliths in South African kimberlite pipes and their petrogenesis. Contributions to Mineralogy and Petrology 25, 163–184. https://doi.org/10.1007/BF00371129

Chevychelov, V.Y., Botcharnikov, R.E., Holtz, F., 2008. Experimental study of fluorine and chlorine contents in mica (biotite) and their partitioning between mica, phonolite melt, and fluid. Geochemistry International 46, 1081–1089. https://doi.org/10.1134/S0016702908110025

Condamine, P., Médard, E., 2014. Experimental melting of phlogopite-bearing mantle at 1 GPa: Implications for potassic magmatism. Earth and Planetary Science Letters 397, 80–92. https://doi.org/10.1016/j.epsl.2014.04.027

Condamine, P., Médard, E., Devidal, J.L., 2016. Experimental melting of phlogopite-peridotite in the garnet stability field. Contributions to Mineralogy and Petrology 171, 1–26. https://doi.org/10.1007/s00410-016-1306-0

Contini, S., Venturelli, G., Toscani, L., Capedri, S., Barbieri, M., 1993. Cr-Zr-armalcolite-bearing lamproites of Cancarix, SE Spain. Mineralogical Magazine 57, 203–216. https://doi.org/10.1180/minmag.1993.057.387.02

Dalou, C., Koga, K.T., Shimizu, N., Boulon, J., Devidal, J.L., 2012. Experimental determination of F and Cl partitioning between lherzolite and basaltic melt. Contributions to Mineralogy and Petrology 163, 591–609. https://doi.org/10.1007/s00410-011-0688-2

Dasgupta, R., Hirschmann, M.M., 2010. The deep carbon cycle and melting in Earth's interior. Earth and Planetary Science Letters 298, 1–13. https://doi.org/10.1016/j.epsl.2010.06.039

Dasgupta, R., Hirschmann, M.M., 2006. Melting in the Earth's deep upper mantle caused by carbon dioxide. Nature 440, 659–662. https://doi.org/10.1038/nature04612

Dasgupta, R., Hirschmann, M.M., Stalker, K., 2006. Immiscible transition from carbonate-rich to silicate-rich melts in the 3 GPa melting interval of eclogite + CO2 and genesis of silica-undersaturated ocean island lavas. Journal of Petrology 47, 647–671. https://doi.org/10.1093/petrology/egi088

Dasgupta, R., Mallik, A., Tsuno, K., Withers, A.C., Hirth, G., Hirschmann, M.M., 2013. Carbon-dioxide-rich silicate melt in the Earth's upper mantle. Nature 493, 211–215. https://doi.org/10.1038/nature11731

Dawson, J.B., 1971. Advances in kimberlite geology. Earth Science Reviews 7, 187–214. https://doi.org/10.1016/0012-8252(71)90120-6

Edgar, A.D., Arima, M., 1985. Fluorine and chlorine contents of phlogopites crystallized from ultrapotassic rock compositions in high pressure experiments: implication for halogen reservoirs in source regions. American Mineralogist 70, 529–536.

Edgar, A.D., Arima, M., 1983. Conditions of phlogopite crystallization in ultrapotassic volcanic rocks. Mineralogical Magazine 47, 11–19. https://doi.org/10.1180/minmag.1983.047.342.02

Edgar, A.D., Charbonneau, H.E., 1991. Fluorine-bearing phases in lamproites. Mineralogy and Petrology 44, 125–149. https://doi.org/10.1007/BF01167104

Edgar, A.D., Charbonneau, H.E., Mitchell, R.H., 1992. Phase relations of an armalcolite-phlogopite lamproite from smoky butte, Montana: Applications to lamproite genesis. Journal of Petrology 33, 505–520. https://doi.org/10.1093/petrology/33.3.505

Edgar, A.D., Pizzolato, L.A., 1995. An experimental study of partitioning of fluorine between K-richterite, apatite, phlogopite, and melt at 20 kbar. Contributions to Mineralogy and Petrology 121, 247–257. https://doi.org/10.1007/BF02688240

Edgar, A.D., Pizzolato, L.A., Sheen, J., 1996. Fluorine in igneous rocks and minerals with emphasis on ultrapotassic mafic and ultramafic magmas and their mantle source regions. Mineralogical Magazine 60, 243–257. https://doi.org/10.1180/minmag.1996.060.399.01

Edgar, A.D., Vukadinovic, D., 1993. Potassium-rich clinopyroxene in the mantle: An experimental investigation of a K-rich lamproite up to 60 kbar. Geochimica et Cosmochimica Acta 57, 5063–5072. https://doi.org/10.1016/0016-7037(93)90608-Y

Fabbrizio, A., Schmidt, M.W., Günther, D., Eikenberg, J., 2010. Ra-partitioning between phlogopite and silicate melt and 226Ra/Ba-230Th/Ba isochrons. Lithos 114, 121–131. https://doi.org/10.1016/j.lithos.2009.08.004

Fabbrizio, A., Stalder, R., Hametner, K., Günther, D., 2013. Experimental chlorine partitioning between forsterite, enstatite and aqueous fluid at upper mantle conditions. Geochimica et Cosmochimica Acta 121, 684–700. https://doi.org/10.1016/j.gca.2013.05.026

Fitzpayne, A., Giuliani, A., Hergt, J., Phillips, D., Janney, P., 2018a. New geochemical constraints on the origins of MARID and PIC rocks: Implications for mantle metasomatism and mantle-derived potassic magmatism. Lithos 318–319, 478–493. https://doi.org/10.1016/j.lithos.2018.08.036

Fitzpayne, A., Giuliani, A., Phillips, D., Hergt, J., Woodhead, J.D., Farquhar, J., Fiorentini, M.L., Drysdale, R.N., Wu, N., 2018b. Kimberlite-related metasomatism recorded in MARID and PIC mantle xenoliths. Mineralogy and Petrology 112, 71–84. https://doi.org/10.1007/s00710-018-0573-z

Flemetakis, S., Klemme, S., Stracke, A., Genske, F., Berndt, J., Rohrbach, A., 2021. Constraining the presence of amphibole and mica in metasomatized mantle sources through halogen partitioning experiments. Lithos 380–381, 105859. https://doi.org/10.1016/j.lithos.2020.105859

Foley, S., 1992. Vein-plus-wall-rock melting mechanisms in the lithosphere and the origin of potassic alkaline magmas. Lithos 28, 435–453. https://doi.org/10.1016/0024-4937(92)90018-T

Foley, S., 1991. High-pressure stability of the fluor- and hydroxy-endmembers of pargasite and K-richterite. Geochimica et Cosmochimica Acta 55, 2689–2694. https://doi.org/10.1016/0016-7037(91)90386-J

Foley, S.F., 1993. An experimental study of olivine lamproite: First results from the diamond stability field. Geochimica et Cosmochimica Acta 57, 483–489. https://doi.org/10.1016/0016-7037(93)90448-6

Foley, S.F., 1990a. Experimental constraints on phlogopite chemistry in lamproites: 2. Effect of pressure-temperature variations. European Journal of Mineralogy 2, 327–342. https://doi.org/10.1127/ejm/2/3/0327

Foley, S.F., 1990b. A review and assessment of experiments on Kimberlites, Lamproites and Lamprophyres as a guide to their Origin. Proceedings of the Indian Academy of Sciences - Earth and Planetary Sciences 99, 57–80. https://doi.org/10.1007/BF02871896

Foley, S.F., 1989a. Experimental constraints on phlogopite chemistry in lamproites: 1. The effect of water activity and oxygen fugacity. European Journal of Mineralogy 1, 411–426. https://doi.org/10.1127/ejm/1/3/0411

Foley, S.F. 1989b The genesis of lamproitic magmas in a reduced, fluorine-rich mantle. In: (eds. J. Ross et al.) *Kimberlites and related rocks* Vol. 1, Blackwell, Melbourne, pp.616-632

Foley, S.F., Taylor, W.R., Green, D.H., 1986. The role of fluorine and oxygen fugacity in the genesis of the ultrapotassic rocks. Contributions to Mineralogy and Petrology 94, 183–192. https://doi.org/10.1007/BF00592935

Foley, S.F., Venturelli, G., Green, D.H., Toscani, L., 1987. The ultrapotassic rocks: Characteristics, classification, and constraints for petrogenetic models. Earth Science Reviews 24, 81–134. https://doi.org/10.1016/0012-8252(87)90001-8

Foley, S.F., Yaxley, G.M., Rosenthal, A., Buhre, S., Kiseeva, E.S., Rapp, R.P., Jacob, D.E., 2009. The composition of near-solidus melts of peridotite in the presence of CO2 and H2O between 40 and 60 kbar. Lithos 112S, 274–283. https://doi.org/10.1016/j.lithos.2009.03.020

Förster, M.W., Prelević, D., Schmück, H.R., Buhre, S., Marschall, H.R., Mertz-Kraus, R., Jacob, D.E., 2018. Melting phlogopite-rich MARID: Lamproites and the role of alkalis in olivine-liquid Ni-partitioning. Chemical Geology 476, 429–440. https://doi.org/10.1016/j.chemgeo.2017.11.039

Fritschle, T., Prelević, D., Foley, S.F., Jacob, D.E., 2013. Petrological characterization of the mantle source of Mediterranean lamproites: Indications from major and trace elements of phlogopite. Chemical Geology 353, 267–279. https://doi.org/10.1016/j.chemgeo.2012.09.006

Funk, S.P., Luth, R.W., 2013. Melting phase relations of a mica-clinopyroxenite from the Milk River area, southern Alberta, Canada. Contributions to Mineralogy and Petrology 166, 393–409. https://doi.org/10.1007/s00410-013-0881-6

667 Girnis, A. v., Brey, G.P., Ryabchikov, I.D., 1995. Origin of Group 1A kimberlites: Fluid-
668 saturated melting experiments at 45-55 kbar. Earth and Planetary Science Letters 134,
669 283–296. https://doi.org/10.1016/0012-821X(95)00120-2
670 Green, D.H., 2015. Experimental petrology of peridotites, including effects of water and
671 carbon on melting in the Earth's upper mantle. Physics and Chemistry of Minerals 42,
672 95–122. https://doi.org/10.1007/s00269-014-0729-2
673 Green, D.H., 1990. The role of oxidation-reduction and C-H-O fluids in determining melting
674 conditions and magma compositions in the upper mantle. Proceedings of the Indian
675 Academy of Sciences - Earth and Planetary Sciences 99, 153–165.
676 https://doi.org/10.1007/BF02871903
677 Green, D.H., Hibberson, W.O., Kovács, I., Rosenthal, A., 2010. Water and its influence on
678 the lithosphere-asthenosphere boundary. Nature 467, 448–451.
679 https://doi.org/10.1038/nature09369
680 Green, D.H., Hibberson, W.O., Rosenthal, A., Kovács, I., Yaxley, G.M., Falloon, T., Brink,
681 F., 2014. Experimental study of the influence of water on melting and phase
682 assemblages in the upper mantle. Journal of Petrology 55, 2067–2096.
683 https://doi.org/10.1093/petrology/egu050
684 Green, T.H., Blundy, J.D., Adam, J., Yaxley, G.M., 2000. SIMS determination of trace
685 element partition coefficients between garnet, clinopyroxene and hydrous basaltic
686 liquids at 2–7.5 GPa and 1080–1200°C. Lithos 53, 165–187.
687 https://doi.org/10.1016/S0024-4937(00)00023-2
688 Grégoire, M., Bell, D., le Roex, A., 2002. Trace element geochemistry of phlogopite-rich
689 mafic mantle xenoliths: Their classification and their relationship to phlogopite-bearing
690 peridotites and kimberlites revisited. Contributions to Mineralogy and Petrology 142,
691 603–625. https://doi.org/10.1007/s00410-001-0315-8
692 Grützner, T., Kohn, S.C., Bromiley, D.W., Rohrbach, A., Berndt, J., Klemme, S., 2017. The
693 storage capacity of fluorine in olivine and pyroxene under upper mantle conditions.
694 Geochimica et Cosmochimica Acta 208, 160–170.
695 https://doi.org/10.1016/j.gca.2017.03.043
696 Guo, J., Green, T.H., 1990. Experimental study of barium partitioning between phlogopite
697 and silicate liquid at upper-mantle pressure and temperature. Lithos 24, 83–95.
698 https://doi.org/10.1016/0024-4937(90)90018-V
699 Hauri, E.H., Gaetani, G.A., Green, T.H., 2006. Partitioning of water during melting of the
700 Earth's upper mantle at H2O-undersaturated conditions. Earth and Planetary Science
701 Letters 248, 715–734. https://doi.org/10.1016/j.epsl.2006.06.014
702 Holland, T.J.B., 1980. The reaction albite= jadeite+ quartz determined experimentally in the
703 range 600-1200 degrees C. American Mineralogist 65, 129–134.
704 Jaques, A.L., Lewis, J.D., Smith, C.B., 1986. The Kimberlites and Lamproites of Western
705 Australia. Geological Survey of Western Australia Bulletin 132, 357.
706 Jaques, A.L., Lewis, J.D., Smith, C.B., Gregory, G.P., Ferguson, J., Chappell, B.W.,
707 McCulloch, M.T., 1984. The diamond-bearing ultrapotassic (lamproitic) rocks of the
708 West Kimberley region, Western Australia. Kimberlites I: kimberlites and related rocks
709 1, 225–254.
710 Joachim, B., Stechern, A., Ludwig, T., Konzett, J., Pawley, A., Ruzié-Hamilton, L., Clay, P.
711 L., Burgess, R., & Ballentine, C. J. (2017). Effect of water on the fluorine and chlorine
712 partitioning behavior between olivine and silicate melt. *Contributions to Mineralogy and*
713 *Petrology*, *172*(4), 15. https://doi.org/10.1007/s00410-017-1329-1
714 Karato, S.I., 2011. Water distribution across the mantle transition zone and its implications
715 for global material circulation. Earth and Planetary Science Letters 301, 413–423.
716 https://doi.org/10.1016/j.epsl.2010.11.038

Kelley, S.P., 2000. Rapid kimberlite sscent and the significance of Ar-Ar Ages in xenolith phlogopites. Science 289, 609–611. https://doi.org/10.1126/science.289.5479.609

Kinzler, R.J., 1997. Melting of mantle peridotite at pressures approaching the spinel to garnet transition: Application to mid-ocean ridge basalt petrogenesis. Journal of Geophysical Research B: Solid Earth 102, 853–874. https://doi.org/10.1029/96jb00988

Klemme, S., & Stalder, R. (2018). Halogens in the Earth's Mantle: What We Know and What We Don't. In *The Role of Halogens in Terrestrial and Extraterrestrial Geochemical Processes: Surface, Crust, and Mantle* (pp. 847–869). https://doi.org/10.1007/978-3-319-61667-4_14

Koga, K.T., Rose-Koga, E.F., 2018. Le fluor dans la Terre et le système solaire, d'où vient-il et où peut-on le trouver ? Comptes Rendus Chimie 21, 749–756. https://doi.org/10.1016/j.crci.2018.02.002

Konzett, J., Sweeney, R.J., Thompson, A.B., Ulmer, P., 1997. Potassium amphibole stability in the upper mantle: An experimental study in a peralkaline KNCMASH system to 8·5 GPa. Journal of Petrology 38, 537–568. https://doi.org/10.1093/petroj/38.5.537

Kovács, I., Green, D.H., Rosenthal, A., Hermann, J., O'neill, H.S.C., Hibberson, W.O., Udvardi, B., 2012. An experimental study of water in nominally anhydrous minerals in the upper mantle near the water-saturated solidus. Journal of Petrology 53, 2067–2093. https://doi.org/10.1093/petrology/egs044

Krausz, K., 1974. Potassium-barium exchange in phlogopite. Canadian Mineralogist 12, 394–398.

Lambart, S., Baker, M.B., Stolper, E.M., 2016. The role of pyroxenite in basalt genesis: Melt-PX, a melting parameterization for mantle pyroxenites between 0.9 and 5 GPa. Journal of Geophysical Research: Solid Earth 121, 5708–5735. https://doi.org/10.1002/2015JB012762

Lambart, S., Laporte, D., Schiano, P., 2013. Markers of the pyroxenite contribution in the major-element compositions of oceanic basalts: Review of the experimental constraints. Lithos 160–161, 14–36. https://doi.org/10.1016/j.lithos.2012.11.018

Laporte, D., Lambart, S., Schiano, P., Ottolini, L., 2014. Experimental derivation of nepheline syenite and phonolite liquids by partial melting of upper mantle peridotites. Earth and Planetary Science Letters 404, 319–331. https://doi.org/10.1016/j.epsl.2014.08.002

Latourrette, T., Hervig, R.L., Holloway, J.R., 1995. Trace element partitioning between amphibole, phlogopite, and basanite melt, Earth and Planetary Science Letters 135, 13-30.

Li, X., Zhang, C., Behrens, H., Holtz, F., 2018. Fluorine partitioning between titanite and silicate melt and its dependence on melt composition: experiments at 50–200 MPa and 875–925°C. European Journal of Mineralogy 30, 33–44. https://doi.org/10.1127/ejm/2017/0029-2689

Melzer, S., Foley, S.F., 2000. Phase relations and fractionation sequences in potassic magma series modelled in the system $CaMgSi_2O_6$-$KAlSiO_4$-Mg_2SiO_4-SiO_2-F_2O_{-1} at 1 bar to 18 kbar. Contributions to Mineralogy and Petrology 138, 186–197.

Mitchell, R.H., 2021. Potassic Alkaline Rocks: Leucitites, Lamproites, and Kimberlites. Encyclopedia of Geology 215–239. https://doi.org/10.1016/b978-0-12-409548-9.12482-0

Mitchell, R.H., 1995. Melting experiments on a sanidine phlogopite lamproite at 4-7 gpa and their bearing on the sources of lamproitic magmas. Journal of Petrology 36, 1455–1474. https://doi.org/10.1093/petrology/36.5.1455

765 Mitchell, R.H., 1981. Titaniferous phlogopites from the leucite lamproites of the West
766 Kimberley area, Western Australia. Contributions to Mineralogy and Petrology 76, 243–
767 251. https://doi.org/10.1007/BF00371964
768 Mitchell, R.H., Bergman, S.C., 1991. Description of Lamproite Occurrences, in: Petrology of
769 Lamproites. Springer US, Boston, MA, pp. 39–102. https://doi.org/10.1007/978-1-4615-
770 3788-5_3
771 Murphy, D.T., Collerson, K.D., Kamber, B.S., 2002. Lamproites from gaussberg, Antarctica:
772 Possible transition zone melts of archaean subducted sediments. Journal of Petrology 43,
773 981–1001. https://doi.org/10.1093/petrology/43.6.981
774 Novella, D., Frost, D.J., 2014. The composition of hydrous partial melts of garnet peridotite
775 at 6GPa: Implications for the origin of group II Kimberlites. Journal of Petrology 55,
776 2097–2124. https://doi.org/10.1093/petrology/egu051
777 Pérez-Valera, L.A., Rosenbaum, G., Sánchez-Gómez, M., Azor, A., Fernández-Soler, J.M.,
778 Pérez-Valera, F., Vasconcelos, P.M., 2013. Age distribution of lamproites along the
779 Socovos Fault (southern Spain) and lithospheric scale tearing. Lithos 180–181, 252–263.
780 https://doi.org/10.1016/j.lithos.2013.08.016
781 Perrillat, J.P., Daniel, I., Lardeaux, J.M., Cardon, H., 2003. Kinetics of the coesite-quartz
782 transition: Application to the exhumation of ultrahigh-pressure rocks. Journal of
783 Petrology 44, 773–788. https://doi.org/10.1093/petrology/44.4.773
784 Pintér, Z., Foley, S.F., Yaxley, G.M., Rosenthal, A., Rapp, R.P., Lanati, A.W., Rushmer, T.,
785 2021. Experimental investigation of the composition of incipient melts in upper mantle
786 peridotites in the presence of CO2 and H2O. Lithos 396–397.
787 https://doi.org/10.1016/j.lithos.2021.106224
788 Prelević, D., Akal, C., Foley, S.F., Romer, R.L., Stracke, A., van den Bogaard, P., 2012.
789 Ultrapotassic mafic rocks as geochemical proxies for post-collisional dynamics of
790 orogenic lithospheric mantle: The case of southwestern Anatolia, Turkey. Journal of
791 Petrology 53, 1019–1055. https://doi.org/10.1093/petrology/egs008
792 Prelević, D., Foley, S.F., Romer, R.L., Cvetković, V., Downes, H., 2005. Tertiary
793 ultrapotassic volcanism in Serbia: Constraints on petrogenesis and mantle source
794 characteristics. Journal of Petrology 46, 1443–1487.
795 https://doi.org/10.1093/petrology/egi022
796 Prelević, D., Jacob, D.E., Foley, S.F., 2013. Recycling plus: A new recipe for the formation
797 of Alpine-Himalayan orogenic mantle lithosphere. Earth and Planetary Science Letters
798 362, 187–197. https://doi.org/10.1016/j.epsl.2012.11.035
799 Richardson, S.H., Erlank, A.J., Hart, S.R., 1985. Kimberlite-borne garnet peridotite xenoliths
800 from old enriched subcontinental lithosphere. Earth and Planetary Science Letters 75,
801 116–128. https://doi.org/10.1016/0012-821X(85)90094-9
802 Roberge, M., Bureau, H., Bolfan-Casanova, N., Frost, D.J., Raepsaet, C., Surble, S., Khodja,
803 H., Auzende, A.L., Fiquet, G., 2015. Is the transition zone a deep reservoir for fluorine?
804 Earth and Planetary Science Letters 429, 25–32.
805 https://doi.org/10.1016/j.epsl.2015.07.051
806 Safonov, O., Butvina, V., Limanov, E., 2019. Phlogopite-forming reactions as indicators of
807 metasomatism in the lithospheric mantle. Minerals 9, 1–18.
808 https://doi.org/10.3390/min9110685
809 Schmidt, K.H., Bottazzi, P., Vannucci, R., Mengel, K., 1999. Trace element partitioning
810 between phlogopite, clinopyroxene and leucite lamproite melt, Earth and Planetary
811 Science Letters 168, 287-299.
812 Shaw, C.S.J., Penczak, R.S., 1996. Barium- and titanium-rich biotite and phlogopite from the
813 Western and Eastern Gabbro, Coldwell alkaline complex, Northwestern Ontario.
814 Canadian Mineralogist 34, 967–975.

Sheppard, S., & Taylor, W. R. (2019). Barium-Rich, Olivine-Mica Lamprophyres with Affinities to Lamproites, from the Mt Bundey Area, Northern Territory, Australia. *International Kimberlite Conference Extended Abstracts: 1991*, *February*. https://doi.org/10.29173/ikc2571

Solovova, I.P., Girnis, A. v., Ryabchikov, I.D., Kononkova, N.N., 2009. Mechanisms of formation of barium-rich phlogopite and strontium-rich apatite during the final stages of alkaline magma evolution. Geochemistry International 47, 578–591. https://doi.org/10.1134/S0016702909060044

Stracke, A., Zindler, A., Salters, V.J.M., McKenzie, D., Grönvold, K., 2003. The dynamics of melting beneath Theistareykir, northern Iceland. Geochemistry, Geophysics, Geosystems 4. https://doi.org/10.1029/2002GC000347

Sweeney, R.J., Prozesky, V., Przybylowicz, W., 1995. Selected trace and minor element partitioning between peridotite minerals and carbonatite melts at 18-46 kb pressure, Geochimica et Cosmochimica Acta 59, 3671-3683.

Sweeney, R.J., Thompson, A.B., Ulmer, P., 1993. Phase relations of a natural MARID composition and implications for MARID genesis, lithospheric melting and mantle metasomatism. Contributions to Mineralogy and Petrology 115, 225–241. https://doi.org/10.1007/BF00321222

Tappe, S., Foley, S.F., Kjarsgaard, B.A., Romer, R.L., Heaman, L.M., Stracke, A., Jenner, G.A., 2008. Between carbonatite and lamproite-Diamondiferous Torngat ultramafic lamprophyres formed by carbonate-fluxed melting of cratonic MARID-type metasomes. Geochimica et Cosmochimica Acta 72, 3258–3286. https://doi.org/10.1016/j.gca.2008.03.008

Taylor, W.R., Foley, S.F., 1989. Improved oxygen-buffering techniques for C-O-H fluid-saturated experiments at high pressure. Journal of Geophysical Research 94, 4146-4158.

Thibault, Y., Edgar, A.D., Lloyd, F.E., 1992. Experimental investigation of melts from a carbonated phlogopite lherzolite: implications for metasomatism in the continental lithospheric mantle. American Mineralogist 77, 784–794.

Tollan, P.M.E., O'Neill, H.S.C., Hermann, J., Benedictus, A., Arculus, R.J., 2015. Frozen melt-rock reaction in a peridotite xenolith from sub-arc mantle recorded by diffusion of trace elements and water in olivine. Earth and Planetary Science Letters 422, 169–181. https://doi.org/10.1016/j.epsl.2015.03.055

Vukadinovic, D., Edgar, A.D., 1993. Phase relations in the phlogopite-apatite system at 20 kbar; implications for the role of fluorine in mantle melting. Contributions to Mineralogy and Petrology 114, 247–254. https://doi.org/10.1007/BF00307759

Walter, M.J., 1998. Melting of garnet peridotite and the origin of komatiite and depleted lithosphere. Journal of Petrology 39, 29–60. https://doi.org/10.1093/petroj/39.1.29

Wang, Y., Foley, S.F., Prelević, D., 2017. Potassium-rich magmatism from a phlogopite-free source. Geology 45, 467–470. https://doi.org/10.1130/G38691.1

Waters, F.G., 1987. A suggested origin of MARID xenoliths in kimberlites by high pressure crystallization of an ultrapotassic rock such as lamproite. Contributions to Mineralogy and Petrology 95, 523–533. https://doi.org/10.1007/BF00402210

Wendlandt, R.F., 1977. Barium-phlogopite from Haystack Butte, Highwood Mountains, Montana. Carnegie Institution of Washington Year Book 76, 534-539.

Zou, H., 1998. Trace element fractionation during modal and nonmodal dynamic melting and open-system melting: a mathematical treatment. Geochimica et Cosmochimica Acta 62, 1937–1945. https://doi.org/10.1016/S0016-7037(98)00115-X

This is the peer-reviewed, final accepted version for American Mineralogist, published by the Mineralogical Society of America.
The published version is subject to change. Cite as Authors (Year) Title. American Mineralogist, in press.
DOI: https://doi.org/10.2138/am-2022-8289. http://www.minsocam.org/

881 T**able 1. Compositions of starting materials in oxide weight percent.**
882

	OL	LL	WK1	Gauss
SiO2	43.8	51.4	46.71	50.7
TiO2	3.9	3.45	7.15	2.38
Al2O3	4.5	9.95	5.29	9.9
FeO	8.67	6.1	7.88	5.97
MnO	0.17	0.09	0.11	0.09
MgO	23.8	8.03	9.31	8.12
CaO	5.08	4.67	3.42	4.75
Na2O	0.58	1.67	0.72	1.71
K2O	5.08	11.76	7.84	11.52
P2O5	1.64	1.5	1.62	1.45
BaO	1.75	0.63	1.49	0.66
SrO	0.15	0.23	0.2	0.09
ZrO2	0.15	0.14	0.27	0.1
Cr2O3	0.17	0.1	0.07	0.08
NiO	0.13	0.03	0.04	0.03
F	0.53	0.33	0.39	

883
884
885 **OL: olivine lamproite, LL: leucite lamproite, WK1: West Kimberley, Australian lamproite, Gauss: Gaussberg, Antarctican leucite lamproite.**
886
887
888
889
890
891
892
893
894

895 **Table 2. Experimental run conditions and products; experiments are ordered by increasing experimental temperature.**
896

Run No.	Starting mix	P (kbar)	T (°C)	t (hr)	Fluid H_2O # CO_2	Fluid H_2O # CH_4	Phases present
T-1835	Olivine Lamproite	20	1050	10		82	Phl, Ol, L
T-1832	Olivine Lamproite	20	1050	10		55	PHl, Ol, L
T-1711	Olivine Lamproite	20	1100	10		75	Phl, Ol, L
T-1695	Olivine Lamproite	30	1100	2		81	Phl, Ol, L
T-1885	Olivine Lamproite	35	1100	3.5		75	Phl, Opx, Ru, L
T-1663	Olivine Lamproite	20	1150	2		82	Phl, Ol, L
T-1645	Olivine Lamproite	30	1150	2		86	Phl, Ol, L
T-1888	Olivine Lamproite	35	1150	2.5		*	Phl, Opx, Ru, L
T-1795	Olivine Lamproite	30	1200	6		51	Phl, Ol, L
T-1951	Leucite lamproite	5	1050	3.5		41	Phl, Ol, Cpx, L
T-1940	Leucite Lamproite	10	1100	2		82	Phl, L
T-1947	Leucite Lamproite	10	1120	2		80	PHL, L
MO21-61	W. Kimberley + 5 wt% H2O	15	1050	15			Phl, L
T-1918	Leucite Lamproite	15	1100	2		80	Phl, L
MO21-59	Gaussberg Lamproite + 10 wt% H2O	15	1100	24			Phl, Cpx, L
MO21-59	Gaussberg Lamproite + 5 wt% H2O	15	1100	24			Phl, Cpx, L
T-1731	Leucite Lamproite	20	1100	2		78	PhL, L
T-1857	Leucite Lamproite	20	1150	2	15		Phl, Opx, Cpx, L
T-1860	Leucite Lamproite	20	1150	2	86		Phl, Cpx, L
T-1869	Leucite Lamproite	25	1050	5		78	Phl, Ru, L
T-1738	Leucite Lamproite	25	1100	2		67	PhL, L
T-1863	Leucite Lamproite	25	1150	2.7		80	Phl, Opx, L
T-1866	Leucite Lamproite	25	1150	2		78	Phl, Ru, L
T-1879	Leucite Lamproite	30	1000	6.5		83	Phl, Ru, L
T-1716	Leucite Lamproite	30	1100	2		68	PhL, L
T-1715	Leucite Lamproite	30	1150	2		62	Phl, L

Fluid compositions are described by molar % water in either a methane-water fluid or carbon dioxide-water fluid; where * is denoted it was not possible to determine the composition of the fluid. Phases present are Phl: phlogopite, Ol: olivine, Cpx: clinopyroxene, Ru: rutile, Opx: orthopyroxene and L: liquid. Experiment MO21-59 and MO21-61 were conducted without a fluid phase.

This is the peer-reviewed, final accepted version for American Mineralogist, published by the Mineralogical Society of America.
The published version is subject to change. Cite as Authors (Year) Title. American Mineralogist, in press.
DOI: https://doi.org/10.2138/am-2022-8289. http://www.minsocam.org/

1000

Table 3. Mineral chemistry of phlogopite

Run No.	T-1835	T-1832	T-1711	T-1695	T-1885	T-1663	T-1645
Starting mix	Olivine Lamproite	Olivine Lamproite	Olivine Lamproite	Olivine Lamproite	Olivine Lamproite	Olivine Lamproite	Olivine Lamproite
n	5	5	5	4	4	3	5
SiO2	37.93 (0.21)	40.41 (0.32)	39.84 (0.32)	40.04 (0.28)	40.25 (0.13)	38.73 (0.15)	40.51 (0.24)
TiO2	1.92 (0.05)	1.94 (0.04)	1.79 (0.10)	1.13 (0.07)	1.55 (0.08)	2.28 (0.01)	1.13 (0.06)
Al2O3	16.28 (0.26)	13.83 (0.20)	14.29 (0.16)	14.27 (0.20)	15.38 (0.16)	15.54 (0.11)	13.77 (0.17)
Cr2O3	0.21 (0.04)	0.26 (0.05)	0.39 (0.30)	0.48 (0.10)	0.22 (0.02)	0.71 (0.10)	0.27 (0.05)
FeO	2.97 (0.15)	3.49 (0.12)	3.6 (0.10)	2.97 (0.07)	4.52 (0.07)	3.00 (0.05)	3.72 (0.10)
NiO	-	-	-	-	0.27 (0.02)	0.14 (0.01)	-
MgO	22.52 (0.15)	23.56 (0.23)	23.75 (0.10)	24.49 (0.11)	22.01 (0.09)	23.03 (0.13)	23.81 (0.13)
Na2O	-	-	-	-	0.10 (0.02)	0.15 (0.01)	-
K2O	9.21 (0.16)	9.46 (0.11)	9.62 (0.16)	9.84 (0.08)	9.5 (0.06)	9.55 (0.06)	9.83 (0.16)
BaO	3.18 (0.13)	2.46 (0.10)	1.84 (0.08)	1.75 (0.08)	1.7 (0.13)	2.65 (0.12)	1.80 (0.12)
F	0.476 (0.08)	0.638 (0.05)	0.66 (0.04)	0.492 (0.05)	0.43 (0.01)	0.71 (0.01)	0.59 (0.05)
Total	94.75 (0.37)	96.05 (0.82)	95.77 (0.49)	95.46 (0.15)	95.95 (0.14)	96.54 (0.37)	95.43 (0.29)
Mg#	93.11 (0.35)	92.32 (0.24)	92.17 (0.23)	93.63 (0.15)	89.67 (0.11)	93.18 (0.14)	91.94 (0.21)
K/Al	0.612 (0.02)	0.741 (0.01)	0.729 (0.02)	0.747 (0.01)	0.67 (0.01)	0.67 (0.01)	0.773 (0.02)
On the basis of 22 O							
Si	5.47	5.72	5.64	5.68	5.70	5.47	5.76
Ti	0.21	0.21	0.19	0.12	0.16	0.24	0.12
Al	2.77	2.31	2.38	2.39	2.57	2.59	2.31
Cr	0.02	0.03	0.04	0.05	0.02	0.08	0.03

This is the peer-reviewed, final accepted version for American Mineralogist, published by the Mineralogical Society of America.
The published version is subject to change. Cite as Authors (Year) Title. American Mineralogist, in press.
DOI: https://doi.org/10.2138/am-2022-8289. http://www.minsocam.org/

Fe	0.36	0.41	0.43	0.35	0.54	0.35	0.44
Ni					0.03	0.02	
Mg	4.84	4.97	5.01	5.18	4.65	4.85	5.04
Na	0.02	0.00	0.00	0.00	0.03	0.04	0.00
K	1.69	1.71	1.74	1.78	1.72	1.72	1.78
Ba	0.18	0.14	0.10	0.10	0.09	0.15	0.10
F	0.22	0.29	0.30	0.22	0.19	0.32	0.27
SUM	15.78	15.76	15.83	15.87	15.71	15.83	15.85
Total Z - Tetrahedral site	8.24	8.03	8.02	8.07	8.27	8.06	8.07
Total Y - Octahedral site	5.43	5.62	5.67	5.70	5.40	5.54	5.63
Total X - Interlayer site	1.89	1.85	1.84	1.88	1.84	1.91	1.88

1020
1021
1022 **Table 3 continued**

T-1888 Olivine Lamproite 2	T-1795 Olivine Lamproite 4	T-1879 Leucite Lamproite 2	T-1951 Leucite lamproite 4	T-1869 Leucite Lamproite 5	T-1940 Leucite Lamproite 4	T-1918 Leucite Lamproite 5	T-1731 Leucite Lamproite 3
40.985 (0.30)	41.38 (0.46)	38.65 (0.58)	40.74 (0.44)	41.02 (0.84)	40.58 (0.28)	40.8 (0.52)	40 (0.28)
2.38 (0.07)	2.58 (0.29)	2.185 (0.04)	3.66 (0.26)	3.48 (0.59)	3.22 (0.13)	2.98 (0.19)	3.02 (0.13)
14.66 (0.06)	13.2 (0.46)	18.15 (0.49)	12.88 (0.17)	13.08 (0.63)	14.09 (0.49)	13.65 (0.22)	13.78 (0.49)
0.086 (0.04)	0.05 (0.01)	0.25(0.02)	0.36 (0.04)	0.56 (0.21)	1.45 (0.28)	0.6 (0.10)	0.32 (0.03)
6.185 (0.19)	4.44 (0.45)	7.87 (0.29)	4.16 (0.17)	4.9 (0.28)	3.89 (0.48)	4.07 (0.24)	5.47 (0.22)
0.10 (0.01)	-	0.03 (0.02)	-	-	0.23 (0.04)	-	-
19.08 (0.30)	21.56 (1.02)	17.11 (0.28)	22.69 (0.28)	19.68 (0.48)	21.96 (0.46)	22.74 (0.22)	20.95 (1.04)
0.12 (0.01)	0.2 (0.02)	0.087 (0.02)	0.18 (0.12)	-	0.122 (0.03)	-	0.133 (0.05)
8.43 (0.05)	9.44 (0.28)	9.94 (0.04)	10.16 (0.19)	10.04 (0.32)	10.17 (0.15)	10.22 (0.18)	10 (0.31)
2.14 (0.06)	2.77 (0.13)	0.90 (0.19)	0.71 (0.08)	0.45 (0.06)	0.45 (0.04)	0.57 (0.06)	0.59 (0.02)
0.39 (0.01)	0.398 (0.05)	0.19 (0..02)	0.558 (0.09)	0.296 (0.02)	0.32 (0.01)	0.462 (0.05)	0.23 (0.03)
94.68 (0.96)	96.02 (1.48)	95.46 (0.12)	96.07 (0.85)	93.51 (1.14)	96.55 (0.51)	96.10 (0.42)	94.66 (2.87)
84.61 (0.19)	89.61 (1.27)	79.50 (0.12)	90.68 (0.38)	87.73 (0.64)	90.96 (1.19)	90.87 (0.54)	87.21 (0.21)
0.62 (0.01)	0.774 (0.03)	0.59 (0.02)	0.854 (0.01)	0.831 (0.03)	0.78 (0.02)	0.811 (0.01)	0.79 (0.01)
5.89	5.89	5.57	5.74	5.94	5.70	5.74	5.76
0.26	0.28	0.24	0.39	0.38	0.34	0.32	0.33
2.48	2.22	3.09	2.14	2.23	2.33	2.26	2.34

0.01	0.01	0.03	0.04	0.06	0.16	0.07	0.04
0.74	0.53	0.95	0.49	0.59	0.46	0.48	0.66
0.01		0.01			0.03		0.01
4.09	4.58	3.68	4.76	4.25	4.60	4.77	4.50
0.03	0.06	0.02	0.05	0.00	0.03	0.00	0.04
1.54	1.72	1.83	1.83	1.85	1.82	1.83	1.84
0.12	0.15	0.05	0.04	0.03	0.02	0.03	0.03
0.18	0.18	0.08	0.25	0.14	0.14	0.21	0.10
15.38	15.60	15.56	15.72	15.46	15.64	15.70	15.66
8.37	8.11	8.66	7.88	8.17	8.03	8.00	8.10
5.11	5.40	4.91	5.68	5.28	5.59	5.64	5.54
1.69	1.93	1.90	1.92	1.88	1.87	1.86	1.91

This is the peer-reviewed, final accepted version for American Mineralogist, published by the Mineralogical Society of America.
The published version is subject to change. Cite as Authors (Year) Title. American Mineralogist, in press.
DOI: https://doi.org/10.2138/am-2022-8289. http://www.minsocam.org/

1041 **Table 3 continued**

T-1738 Leucite Lamproite 5	T-1716 Leucite Lamproite 5	T-1870 Leucite Lamproite 4	T-1947 Leucite Lamproite 6	T-1857 Leucite Lamproite 4	T-1860 Leucite Lamproite 5	T-1863 Leucite Lamproite 5	T-1715 Leucite Lamproite 5
39.2 (0.77)	41.17 (0.66)	43.3 (0.77)	41.13 (0.40)	41.14 (0.52)	41.62 (0.20)	41.75 (0.46)	40.43 (0.49)
2.38 (0.20)	2.37 (0.15)	4.05 (0.72)	2.73 (0.20)	5.72 (0.24)	4.12 (0.11)	3.71 (0.50)	2.47 (0.07)
16.58 (0.71)	14.55 (064)	14.82 (0.61)	13 (0.52)	13.06 (0.35)	13.03 (0.26)	13.00 (0.20)	15.45 (0.45)
0.76 (0.28)	0.61 (0.05)	0.49 (0.21)	0.9 (0.18)	0.37 (0.12)	0.33 (0.04)	0.62 (0.19)	0.6 (0.13)
4.53 (1.97)	4.28 (0.25)	5.66 (0.26)	3.24 (0.12)	5.51 (0.18)	5.71 (0.20)	4.55 (0.33)	5.39 (0.10)
0.11 (0.06)	0.15 (0.03)		-	-	-	-	0.12 (0.01)
21.34 (1.79)	22.29 (0.12)	17.23 (0.13)	22.62 (0.31)	19.32 (0.18)	21.21 (0.05)	20.99 (0.62)	21.08 (0.41)
0.10 (0.01)	0.084 (0.01)	-	-	-	-	-	0.146 (0.03)
10.25 (0.10)	10.29 (0.03)	10.26 (0.13)	10.08 (0.21)	10.09 (0.08)	10.06 (0.33)	10.26 (0.25)	10.26 (0.12)
0.8 (0.09)	0.41 (0.11)	0.55 (0.16)	0.58 (0.04)	1.02 (0.22)	0.68 (0.05)	0.53 (0.09)	0.51 (0.03)
0.18 (0.03)	0.21 (0.01)	0.275 (0.02)	0.478 (0.04)	0.423 (0.03)	0.438 (0.04)	0.426 (0.04)	0.19 (0.03)
96.27 (0.18)	96.46 (0.38)	96.78 (1.02)	94.74 (1.11)	96.65 (0.61)	97.21 (0.16)	95.82 (0.69)	96.68 (0.67)
89.23 (5.04)	90.28 (0.52)	84.43 (0.64)	92.56 (0.23)	86.21(0.28)	86.87 (0.39)	89.15 (0.96)	87.45 (0.16)
0.67 (0.67)	0.77 (0.04)	0.749 (0.04)	0.839 (0.03)	0.836 (0.03)	0.835 (0.04)	0.854 (0.03)	0.72 (0.03
5.55	5.78	6.05	5.84	5.80	5.82	5.89	5.70
0.25	0.25	0.43	0.29	0.61	0.43	0.39	0.26
2.77	2.41	2.44	2.17	2.17	2.15	2.16	2.57

0.09	0.07	0.05	0.10	0.04	0.04	0.07	0.07
0.54	0.50	0.66	0.38	0.65	0.67	0.54	0.64
0.01	0.02						0.01
4.50	4.66	3.59	4.79	4.06	4.42	4.41	4.43
0.03	0.02	0.00	0.00	0.00	0.00	0.00	0.04
1.85	1.84	1.83	1.83	1.82	1.79	1.85	1.84
0.04	0.02	0.03	0.03	0.06	0.04	0.03	0.03
0.08	0.09	0.12	0.21	0.19	0.19	0.19	0.09
15.71	15.67	15.21	15.65	15.39	15.55	15.53	15.67
8.32	8.19	8.49	8.01	7.97	7.97	8.05	8.27
5.39	5.50	4.73	5.56	5.36	5.56	5.41	5.41
1.92	1.88	1.86	1.86	1.88	1.83	1.88	1.91

1059 **Table 3 continued**

T-1866 Leucite Lamproite	MO21-61 West Kimberley + 5wt% H_2O	MO21-59 Gaussberg + 5 wt% H_2O	MO21-59 Gaussberg + 10wt% H_2O
3	3	5	5
45.92 (0.68)	43.66 (0.23)	42.09 (0.24)	42.25 (0.23)
2.99 (0.37)	2.20 (0.14)	3.31 (0.24)	3.89 (0.19)
16.28 (0.50)	11.77 (0.24)	12.23 (0.08)	12.67 (0.19)
0.05 (0.02)	0.16 (0.01)	0.11 (0.03)	0.31 (0.12)
7.8 (0.53)	1.06 (0.07)	3.39 (0.16)	2.46 (0.08)
-	0.03 (0.02)	0.04 (0.02)	0.02 (0.02)
11.75 (0.83	26.02 (0.22)	24.11 (0.27)	24.03 (0.05)
-	0.07 (0.01)	0.15 (0.03)	0.14 (0.01)
9.69 (0.40)	10.73 (0.03)	10.57 (0.04)	10.62 (0.03)
0.46 (0.04)	0.40 (0.03)	0.23 (0.01)	0.25 (0.02)
0.335 (0.19)	3.16 (0.11)	0.56 (0.04)	0.73 (0.02)
95.16 (0.31)	99.28 (0.03)	96.85 (0.18)	97.41 (0.21)
72.83 (2.19)	97.76 (0.16)	92.68 (0.39)	94.57 (0.17)
0.644 (0.02)	0.99 (0.02)	0.94 (0.01)	0.91 (0.01)
6.45	6.38	5.84	5.80
0.32	0.24	0.35	0.40
2.69	2.03	2.00	2.05

0.01	0.02	0.01	0.03
0.92	0.13	0.39	0.28
2.46	3.06	4.99	4.92
0.00	0.02	0.04	0.04
1.74	2.00	1.87	1.86
0.03	0.02	0.01	0.01
0.15	1.46	0.25	0.32
14.75	15.36	15.76	15.71
9.14	8.41	7.84	7.85
3.71	3.45	5.74	5.63
1.77	2.04	1.92	1.91

Chemical composition of experimental phlogopite in oxide weight percent. n = number of analyses per sample, numbers in parentheses represent 1 standard deviation. Cations on the basis on 22 oxygens.

This is the peer-reviewed, final accepted version for American Mineralogist, published by the Mineralogical Society of America.
The published version is subject to change. Cite as Authors (Year) Title. American Mineralogist, in press.
DOI: https://doi.org/10.2138/am-2022-8289. http://www.minsocam.org/

Table 4. Melt compositions

Run No.	T-1835	T-1832	T-1711	T-1695	T-1885	T-1663	T-1645
Starting mix	Olivine Lamproite	Olivine Lamproite	Olivine Lamproite	Olivine Lamproite	Olivine Lamproite	Olivine Lamproite	Olivine Lamproite
n	9	25	9	10	5	7	10
SiO2	34.45 (1.60)	33.82 (0.78)	38.47 (1.94)	33.69 (2.59)	31.34 (2.69)	39.32 (2.03)	35.6 (2.10)
TiO2	4.56 (1.34)	3.16 (0.34)	3.95 (0.36)	2.11 (1.51)	3.14 (0.52)	4.70 (0.92)	4.07 (1.16)
Al2O3	9.26 (0.83)	16.98 (0.49)	11.51 (1.52)	10.28 (1.34)	10.44 (0.48)	11.65 (1.69)	8.44 (0.77)
Cr2O3	0.03 (0.02)	0.03 (0.02)	0.02 (0.02)	0.02 (0.02)	0.05 (0.02)	0.10 (0.04)	0.11 (0.03)
FeO	7.05 (0.64)	5.01 (0.19)	7.75 (0.82)	6.21 (0.70)	8.58 (0.59)	7.46 (1.22)	8.52 (1.01)
MnO	0.15 (0.04)	0.11 (0.02)	0.12 (0.02)	0.09 (0.03)	0.14 (0.07)	0.12 (0.04)	0.10 (0.03)
NiO	0.02 (0.02)	0.03 (0.02)	0.03 (0.01)	0.02 (0.03)	0.03 (0.02)	0.02 (0.03)	0.02 (0.02)
MgO	9.31 (3.36)	13.08 (0.96)	9.9 (2.36)	8.95 (3.39)	14.18 (0.70)	11.16 (4.91)	12.3 (1.97)
CaO	8.47 (2.82)	4.19 (0.89)	7.24 (1.19)	4.5 (2.28)	4.93 (1.93)	6.61 (3.34)	4.70 (1.37)
Na2O	0.81 (023)	0.65 (0.08)	0.9 (0.16)	0.79 (0.14)	0.42 (0.16)	0.82 (0.31)	0.6 (0.20)
K2O	1.82 (0.71(	2.77 (0.37)	2.96 (0.46)	3.20 (0.76)	3.14 (0.37)	5.2 (1.77)	4.71 (0.78)
P2O5	2.79 (0.98)	1.77 (0.34)	2.28 (0.42)	1.81 (1.32)	1.93 (1.31)	2.82 (1.01)	1.38 (0.52)
BaO	1.21 (0.24)	0.98 (0.16)	1.48 (0.16)	1.74 (0.33)	1.28 (0.20)	2.04 (0.72)	1.67 (0.15)
Cl	0.034 (0.02)	0.05 (0.01)	0.03 (0.01)	0.09 (0.02)	0.03 (0.01)	0.02 (0.01)	0.06 (0.01)
F	0.47 (0.09)	0.40 (0.04	0.57 (0.07)	0.49 (0.07)	0.50 (0.13)	0.75 (0.12)	0.46 (0.04)
Total	80.44 (2.82)	83.04 (1.26)	87.22 (3.24)	73.97 (3.45)	80.14 (2.67)	92.14 (2.57)	82.74 (3.11)
Mg#	68.05 (10.19)	82.25 (1.37)	68.78 (4.45)	70.63 (6.38)	74.64 (1.75)	70.61 (9.64)	71.69 (4.53)
K/Al	0.21 (0.08)	0.18 (0.03)	0.28 (0.04)	0.33 (0.05)	0.33 (0.03)	0.4 (0.22)	0.60 (0.06)

1067

Table 4 continued

T-1888 Olivine Lamproite 8	T-1795 Olivine Lamproite 25	T-1879 Leucite Lamproite 6	T-1951 Leucite lamproite 10	T-1869 Leucite Lamproite 25	T-1940 Leucite Lamproite 25	T-1918 Leucite Lamproite 24	T-1731 Leucite Lamproite 8
33.07 (3.59)	31.94 (1.07)	43.83 (2.96)	51.80 (1.14)	42.21 (2.74)	45.28 (2.6)	46.35 (1.24)	56.51 (2.29)
2.84 (1.15)	2.63 (0.20)	0.07 (0.03)	3.50 (0.39)	2.73 (0.30)	3.77 (0.18)	3.35 (0.17)	2.13 (0.67)
10.62 (0.94)	11.79 (0.46)	9.32 (1.77)	9.52 (0.63)	12.23 (1.04)	11.2 (0.65)	10.82 (0.39)	14.09 (0.46)
0.07 (0.02)	0.06 (0.02)	0.01 (0.01)	0.04 (0.05)	0.05 (0.02)	0.11 (0.03)	0.09 (0.02)	0.02 (0.02)
5.87 (0.84)	18.87 (1.14)	0.22 (0.04)	5.86 (0.61)	5.27 (0.85)	5.98 (0.79)	5.52 (0.59)	1.28 (0.55)
0.07 (0.03)	0.07 (0.02)	0.02 (0.02)	0.10 (0.03)	0.07 (0.02)	0.09 (0.03)	0.08 (0.02)	0.07 (0.02)
0.06 (0.02)	0.01 (0.01)	-	0.02 (0.02)	0.02 (0.02)	0.03 (0.02)	0.03 (0.02)	-
15.26 (1.41)	13.73 (0.78)	-	5.07 (2.24)	6.37 (1.46)	7.73 (2.66)	6.97 (1.16)	0.21 (0.29)
2.24 (1.85)	4.18 (0.53)	2.75 (2.16)	6.96 (1.88)	3.56 (1.53)	4.59 (0.3)	4.38 (1.47)	5.27 (0.60)
0.24 (0.08)	0.7 (0.08)	0.74 (0.11)	1.49 (0.40)	0.65 (0.16)	1.12 (0.06)	1.05 (0.15)	2.02 (0.09)
4.89 (1.01)	3.18 (0.56)	5.52 (0.59)	4.54 (1.16)	6.87 (0.66)	7.01 (0.11)	7.74 (0.42)	8.88 (0.26)
0.76 (0.59)	1.43 (0.25)	1.82 (1.59)	2.25 (0.19)	1.67 (0.43)	1.78 (0.07)	1.66 (0.34)	1.05 (0.70)
1.34 (0.17)	1.31 (0.16)	0.22 (0.09)	0.72 (0.14)	0.47 (0.16)	0.5 (0.07)	0.56 (0.11)	0.49 (0.11)
0.03 (0.01)	0.02 (0.01)	0.08 (0.01)	-	0.04 (0.01)	0.02 (0.01)	0.01 (0.01)	0.01 (0.01)
0.39 (0.08)	0.38 (0.04)	0.19 (0.09)	0.15 (0.04)	0.17 (0.03)	0.19 (0.02)	0.18 (0.02)	0.12 (0.02)
77.44 (4.18)	90.29 (1.43)	64.78 (3.40)	92.02 (1.39)	82.39 (3.50)	89.48 (0.92)	88.80 (1.36)	92.14 (1.01)
82.15 (2.84)	56.44 (2.57)	10.52 (8.45)	57.40 (13.10)	68.01 (1.51)	71.72 (0.37)	69.01 (1.75)	17.96 (12.60)
0.50 (0.08)	0.29 (0.04)	0.65 (0.06)	0.51 (0.12)	0.61 (0.06)	0.69 (0.02)	0.78 (0.05)	0.68 (0.02)

Table 4 continued

T-1738 Leucite Lamproite 9	T-1716 Leucite Lamproite 9	T-1870 Leucite Lamproite 10	T-1857 Leucite Lamproite 26	T-1860 Leucite Lamproite 9	T-1863 Leucite Lamproite 25	T-1715 Leucite Lamproite 10	T-1866 Leucite Lamproite 10
43.77 (3.17)	53.4 (3.9)	49.25 (4.52)	49.05 (0.59)	44.44 (1.45)	50.88 (0.42)	58.42 (3.43)	39.54 (3.94)
2.32 (0.44)	3.0 (0.70)	1.52 (0.08)	3.16 (0.07)	3.42 (0.62)	3.16 (0.07)	0.92 (0.64)	1.25 (0.62)
17.44 (1.03)	14.6 (1.2)	11.88 (1.3)	9.8 (0.09)	10.11 (0.94)	10.20 (0.18)	16.53 (0.64)	9.98 (1.80)
-	-	0.04 (0.04)	0.08 (0.02)	0.16 (0.13)	0.09 (0.02)	0.01 (0.02)	0.03 (0.02)
4.01 (2.47)	0.40 (0.1)	2.80 (1.43)	5.57 (0.16)	6.10 (0.31)	5.17 (0.22)	0.44 (0.48)	2.15 (1.00)
0.04 (0.01)	-	0.07 (0.03)	0.08 (0.02)	0.08 (0.03)	0.07 (0.01)	0.03 (0.02)	0.07 (0.06)
-	-	0.02 (0.02)	0.02 (0.02)	0.04 (0.03)	0.02 (0.02)	0.01 (0.01)	0.01 (0.01)
1.96 (1.76)	0.10 (0.10)	2.32 (2.59)	6.41 (0.36)	8.38 (3.48)	6.59 (0.40)	0.07 (0.15)	1.75 (0.99)
5.65 (2.16)	7.06 (3.2)	3.72 (2.13)	3.91 (0.11)	3.40 (1.16)	4.24 (0.32)	3.46 (0.92)	4.77 (3.25)
2.03 (0.44)	2.23 (0.33)	1.51 (0.44)	1.47 (0.18)	1.77 (0.59)	0.70 (0.14)	2.22 (0.77)	1.27 (0.21)
8.19 (0.51)	5.97 (0.84)	7.20 (0.86)	8.69 (0.43)	10.04 (0.76)	7.78 (0.46)	5.34 (1.75)	5.04 (0.75)
2.21 (0.94)	2.08 (2.22)	1.68 (0.55)	1.59 (0.06)	1.21 (0.34)	1.64 (0.07)	0.29 (0.49)	1.92 (0.71)
0.34 (0.13)	0.10 (0.04)	0.91 (0.37)	0.57 (0.06)	0.58 (0.11)	0.50 (0.06)	0.14 (0.08)	0.69 (0.21)
0.03 (0.01)	0.02 (0.01)	0.03 (0.01)	0.01 (0.010	0.02 (0.01)	0.01 (0.01)	0.02 (0.02)	0.06 (0.02)
0.21 (0.05)	0.02 (0.01)	0.12 (0.02)	0.19 (0.02)	0.20 (0.07)	0.18 (0.02)	0.12 (0.04)	0.14 (0.04)
88.24 (3.17)	89.20 (1.49)	83.06 (3.87)	90.61 (0.37)	89.94 (1.83)	91.24 (0.37)	88.02 (1.16)	68.7 (5.77)
34.69 (19.57)	13.97 (17.12)	50.42 (13.77)	67.18 (1.09)	68.99 (7.32)	69.43 (0.60)	13.76 (12.35)	56.92 (6.14)
0.51 (0.04)	0.45 (0.08)	0.66 (0.04)	0.96 (0.05)	1.09 (0.16)	0.83 (0.05)	0.35 (0.13)	0.56 (0.12)

Table 4 continued

MO21-61 West Kimberley + 5wt% H_2O 4	MO21-59 Gaussberg + 5 wt% H_2O 5	MO21-59 Gaussberg + 10wt% H_2O 5
40.70 (0.51)	51.58 (0.14)	52.78 (0.19)
7.60 (0.40)	3.30 (0.04)	3.24 (0.01)
3.78 (0.36)	9.02 (0.09)	9.67 (0.04)
0.03 (0.01)	-	-
1.20 (0.09)	3.33 (0.03)	2.48 (0.02)
0.12 (0.02)	0.11 (0.01)	0.10 (0.01)
-	0.01 (0.01)	-
11.54 (0.31)	4.81 (0.11)	4.63 (0.03)
14.98 (0.24)	3.56 (0.05)	2.84 (0.04)
0.86 (0.04)	1.72 (0.05)	2.10 (0.04)
6.59 (0.21)	9.21 (0.12)	9.89 (0.04)
2.34 (0.49)	1.82 (0.04)	1.76 (0.06)
1.44 (0.18)	0.78 (0.04)	0.74 (0.03)
-	0.11 (0.01)	0.14 (0.01)
5.19 (0.11)	0.2 (0.02)	0.17 (0.01)
96.36 (0.14)	89.55 (0.16)	90.55 (0.14)
94.5 (0.36)	71.99 (0.37)	76.91 (0.14)
1.9 (0.15)	0.11 (0.01)	1.11 (0.01)

Chemical composition of experimental melts in oxide weight percent. n = number of analyses per sample, numbers in parentheses represent 1 standard deviation.

This is the peer-reviewed, final accepted version for American Mineralogist, published by the Mineralogical Society of America.
The published version is subject to change. Cite as Authors (Year) Title. American Mineralogist, in press.
DOI: https://doi.org/10.2138/am-2022-8289. http://www.minsocam.org/

Table 5. Experimentally determined partition coefficients of F and Ba in phlogopite/melt pairs.

Composition	Experiment	Pressure (kbar)	T (deg C)	D F (Phl/Melt)	1 S.E	D Ba(Phl/Melt)	1 S.E
Olivine Lamproite	T-1835	20	1050	0.96	0.02	2.41	0.14
Olivine Lamproite	T-1832	20	1050	1.61	0.14	2.49	0.24
Olivine Lamproite	T-1711	20	1100	1.26	0.07	1.33	0.07
Olivine Lamproite	T-1695	30	1100	1.05	0.08	0.99	0.11
Olivine Lamproite	T-1885	35	1100	1.07	0.16	1.49	0.06
Olivine Lamproite	T-1663	20	1150	1.11	0.13	1.10	0.04
Olivine Lamproite	T-1645	30	1150	1.31	0.08	1.12	0.03
Olivine Lamproite	T-1888	35	1150	1.10	0.09	1.48	0.18
Olivine Lamproite	T-1795	30	1200	1.06	0.07	2.05	0.13
Average olivine lamproite				1.17	0.09	1.61	0.11
Leucite lamproite	T-1951	5	1050	3.44	0.33	1.20	0.15
Leucite Lamproite	T-1940	10	1100	1.62	0.07	1.03	0.10
Leucite Lamproite	T-1947	10	1120	2.65	0.17	1.19	0.11
Leucite Lamproite	T-1918	15	1100	2.52	0.24	1.21	0.08
Leucite Lamproite	T-1731	20	1100	2.01	0.10	1.10	0.07
Leucite Lamproite	T-1857	20	1150	2.17	0.10	1.85	0.13
Leucite Lamproite	T-1860	20	1150	2.95	0.30	1.10	0.07
Leucite Lamproite	T-1869	25	1050	1.89	0.07	1.06	0.13
Leucite Lamproite	T-1738	25	1100	0.92	0.14	1.95	0.26
Leucite Lamproite	T-1863	25	1150	1.90	0.26	0.52	0.05
Leucite lamproite	T-1866	25	1150	2.97	0.29	0.65	0.01
Leucite Lamproite	T-1879	30	1000	0.99	0.07	3.68	0.43
Leucite Lamproite	T-1716	30	1100	1.42	0.26	3.08	0.42
Leucite Lamproite	T-1715	30	1150	1.49	0.25	3.41	0.48
Average leucite lamproite				1.30	0.19	3.39	0.44

Partition coefficients determined from phlogopite/melt pairs with 1 standard deviation errors reported.

This is the peer-reviewed, final accepted version for American Mineralogist, published by the Mineralogical Society of America.
The published version is subject to change. Cite as Authors (Year) Title. American Mineralogist, in press.
DOI: https://doi.org/10.2138/am-2022-8289. http://www.minsocam.org/

Figure 1

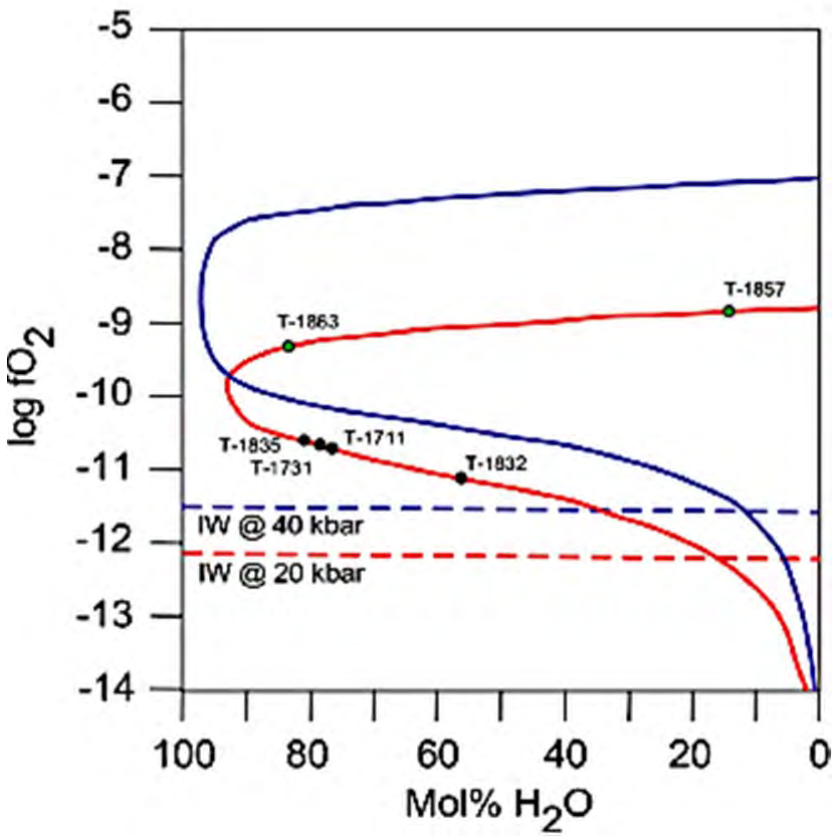

Figure 1. Fluid compositions and oxygen fugacity conditions in the lamproite experiments of Foley, (1989 a,b). The graphite saturation curves for 20 kbar (red) and 40 kbar (blue) show a water maximum at intermediate fO_2, which lies 2-3 log units fO_2 (depending on pressure and temperature) higher than the iron-wüstite buffer (dotted lines). Fluid compositions measured for individual experiments at 20 kbar are shown to illustrate the range of fO_2 in the experiments, which spans around 2 log units. Fluid compositions are listed in Table 2.

This is the peer-reviewed, final accepted version for American Mineralogist, published by the Mineralogical Society of America.
The published version is subject to change. Cite as Authors (Year) Title. American Mineralogist, in press.
DOI: https://doi.org/10.2138/am-2022-8289. http://www.minsocam.org/

Figure 2. Example images of experiments. Primary phlogopites are large, elongated laths free of chemical zonation and are surrounded by quench crystals of melt and phlogopite. (a) Leucite lamproite run T1863, 25kbar at 1150°C, with molar fluid composition 80% water (b) enlarged photomicrograph of quench texture in (a), highlighted by white box. (c) Leucite lamproite run T1866, 25kbar at 1150°C, with molar fluid composition 78% water, (d) enlarged photomicrograph of quench texture in (c), highlighted by white box. (e) Olivine lamproite run T1645 30kbar 1150°C, with a molar fluid composition 86% water, (f) enlarged photomicrograph of quench texture in (e), highlighted by white box.

Figure 2

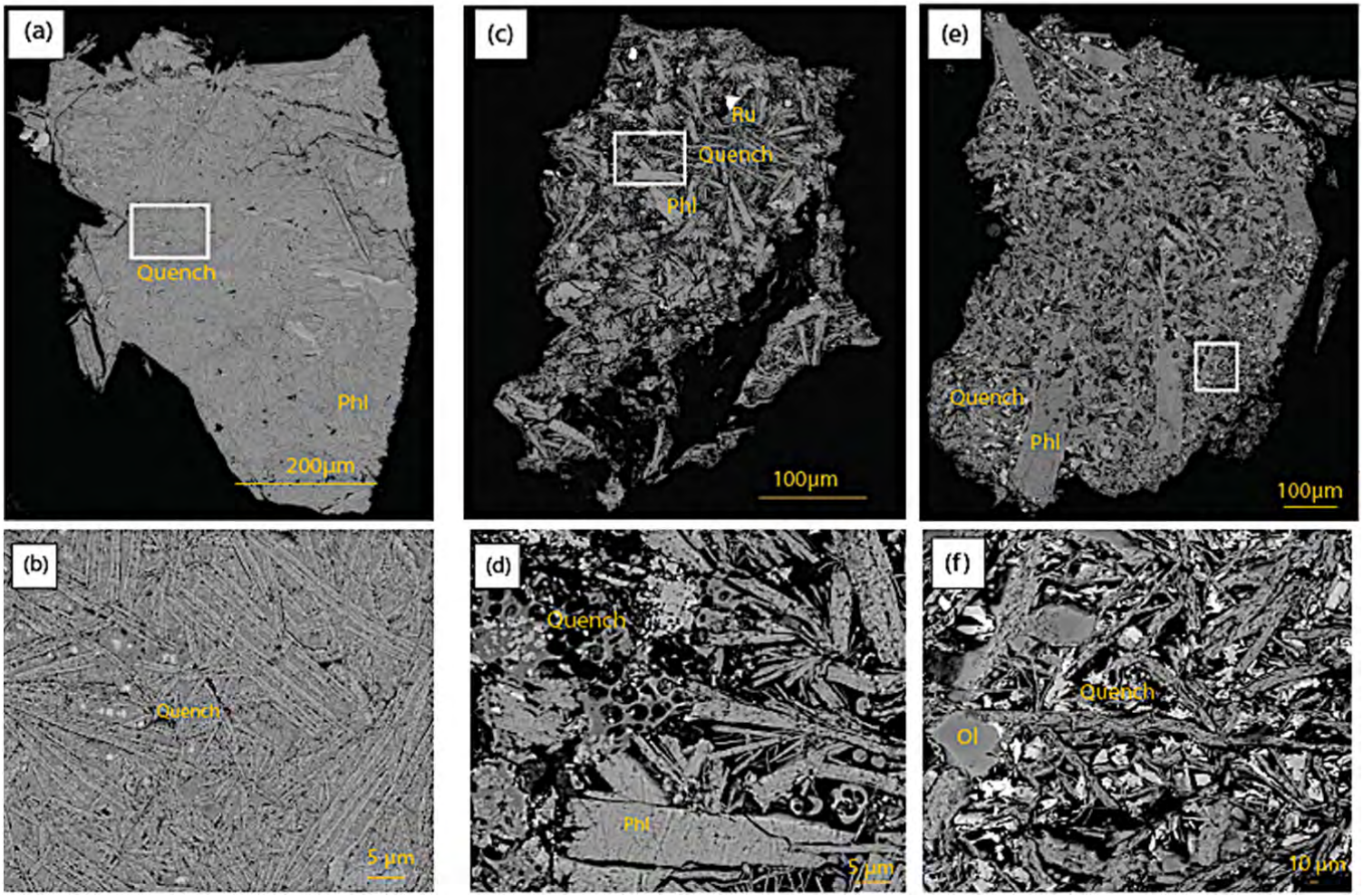

Figure 3. Scanning electron micrograph of run MO21-059, Gaussberg lamproite + 10 wt% H_2O from the GUKO rapid quench piston-cylinder apparatus at Macquarie University. Primary phlogopites are large laths, free from chemical zonation and overgrowth, minor clinopyroxene is observed in this run. Quenched melts produced from the rapid quench piston cylinder are homogenous and free of large quench crystals: enlarged inset shows the presence of tiny phlogopite quench crystals (<2µm), far smaller than those observed using a traditional piston cylinder apparatus.

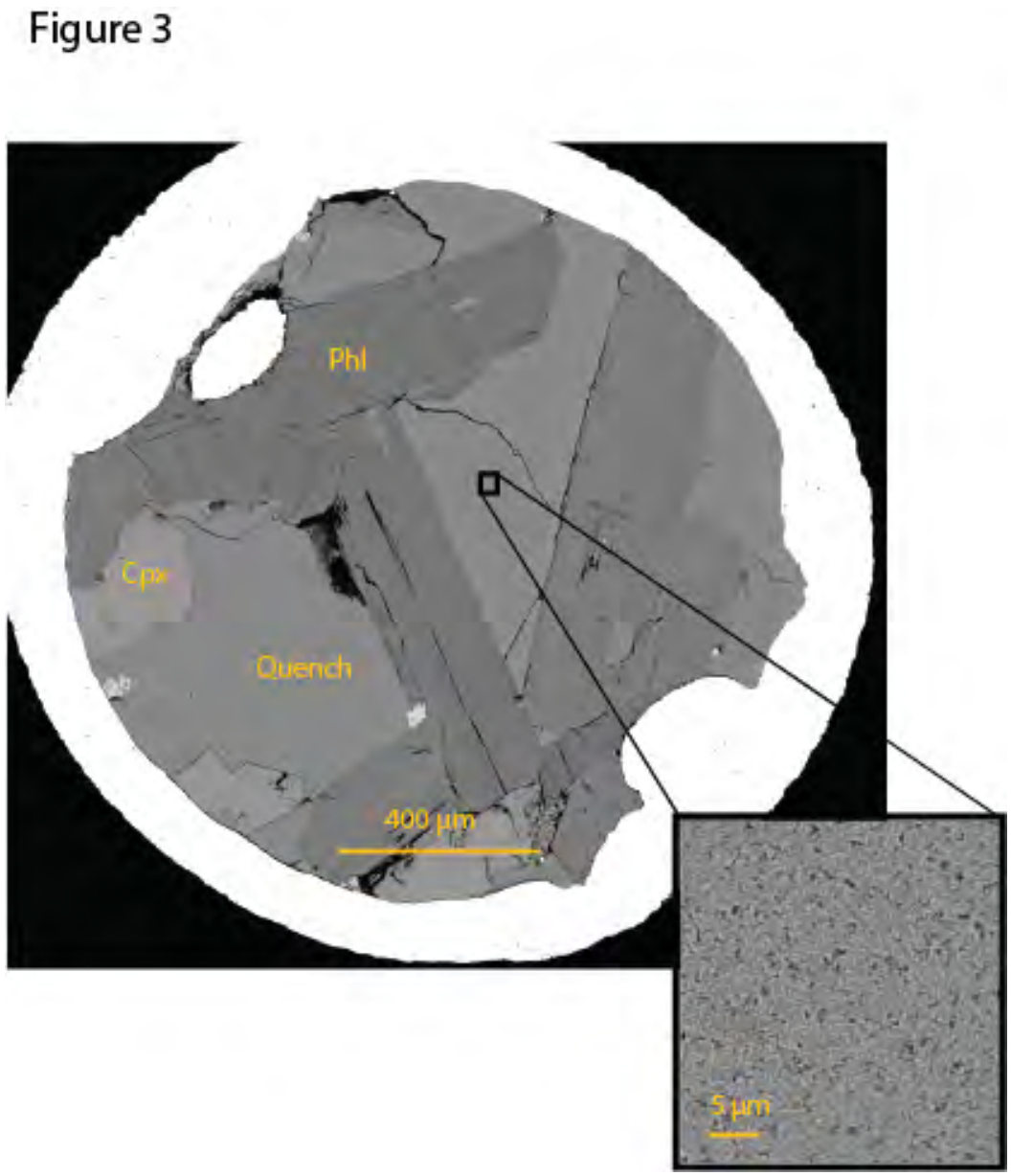

This is the peer-reviewed, final accepted version for American Mineralogist, published by the Mineralogical Society of America.
The published version is subject to change. Cite as Authors (Year) Title. American Mineralogist, in press.
DOI: https://doi.org/10.2138/am-2022-8289. http://www.minsocam.org/

Figure 4. F and BaO content in weight percent in experimental phlogopite from olivine lamproite (a & c) and leucite lamproite (b & d) series experiments. There is a general decrease in both F and BaO content with increasing experimental pressure and temperature. Higher BaO and F are observed in olivine lamproite experiments due to the higher concentrations in the starting materials.

Figure 4

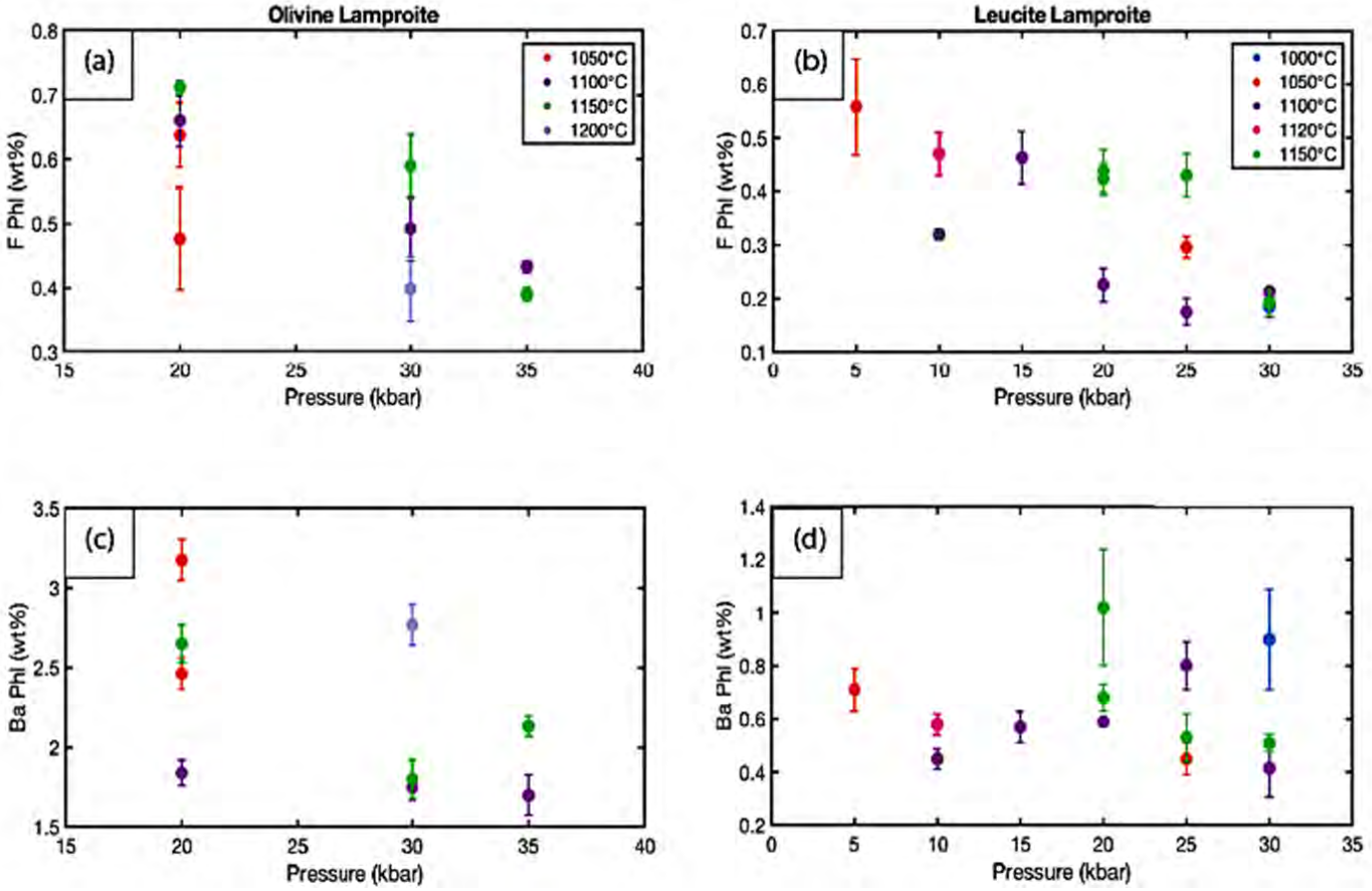

This is the peer-reviewed, final accepted version for American Mineralogist, published by the Mineralogical Society of America.
The published version is subject to change. Cite as Authors (Year) Title. American Mineralogist, in press.
DOI: https://doi.org/10.2138/am-2022-8289. http://www.minsocam.org/

Figure 5. Phlogopite/melt partition coefficients for F and Ba in olivine lamproite (a & c) and leucite lamproite (b & d) experiments. F and Ba are compatible in phlogopite for both melt compositions and generally show increasing partition coefficients with increasing temperature. The wider PT range of leucite lamproite experiments provides more detailed information on the behaviour of F and B partition coefficients, including the opposing pressure effect, whereby F mineral/melt partition coefficients decrease with increasing pressure whilst Ba mineral/melt partition coefficients increase with increasing pressure. Experiments with methane rich fluids (>40% CH_4:H_2O mixtures) are indicated by triangle symbols, all other experiments are circles and have water rich fluids.

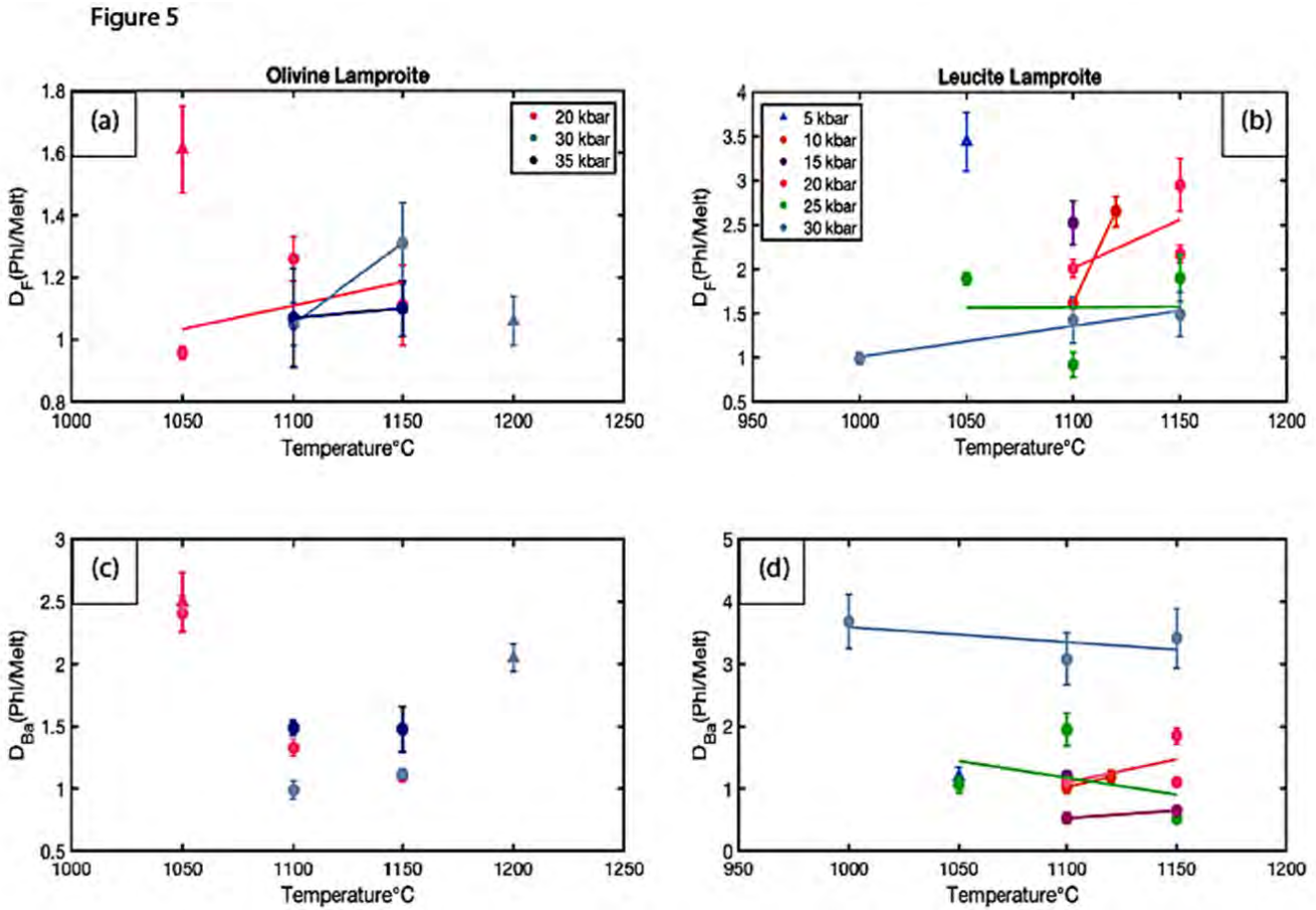

This is the peer-reviewed, final accepted version for American Mineralogist, published by the Mineralogical Society of America.
The published version is subject to change. Cite as Authors (Year) Title. American Mineralogist, in press.
DOI: https://doi.org/10.2138/am-2022-8289. http://www.minsocam.org/

Figure 6. Phlogopite/melt partition coefficients for F and Ba for olivine and leucite lamproite experiments presented here (black symbols) and literature values: pink symbols in (a) are $D_F^{(Phl/Melt)}$ from Edgar and Pizzolato, (1995) for a K-richterite – apatite – phlogopite – melt system. Red symbols in (b) are $D_{Ba}^{(Phl/Melt)}$ from Fabbrizio et al., (2010), pink symbols: Schmidt et al., (1999) and green symbols: Guo and Green, (1990), all of which were determined from leucite lamproite compositions.

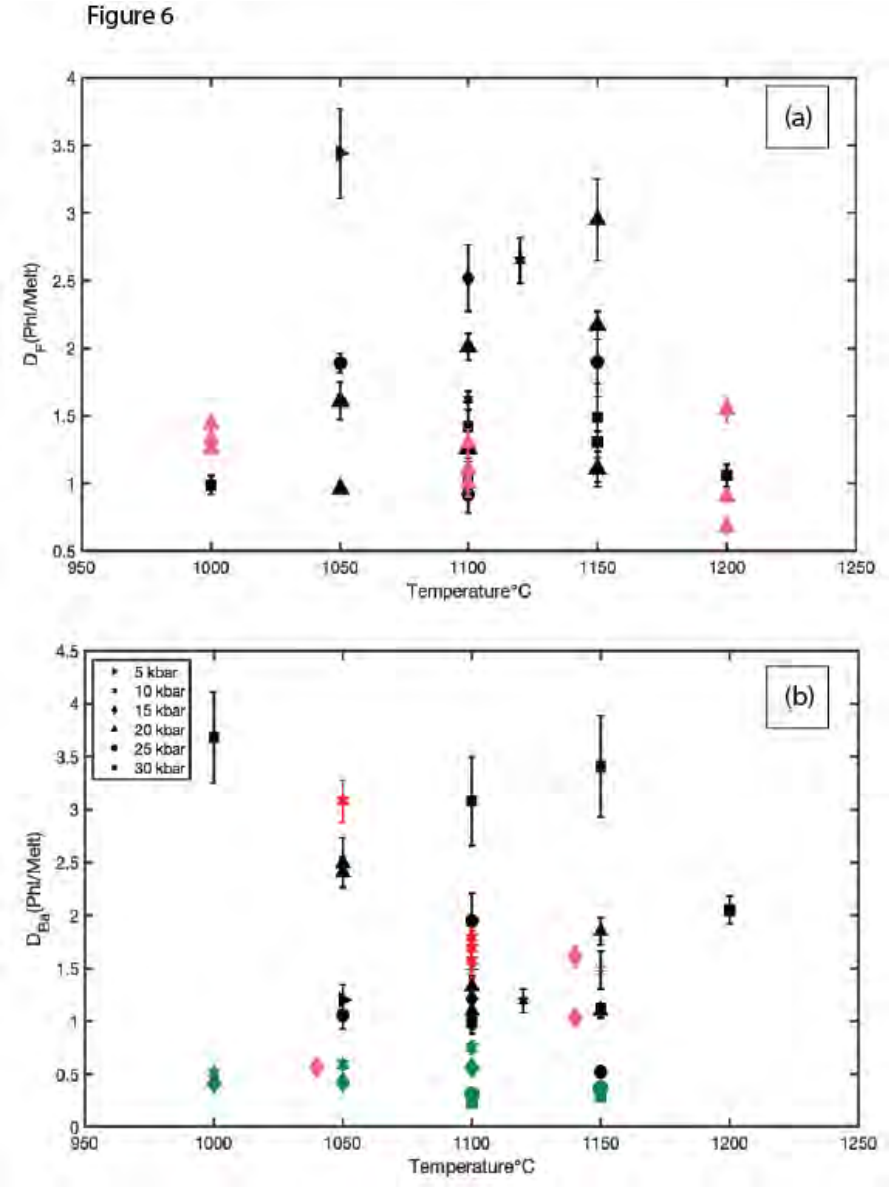

This is the peer-reviewed, final accepted version for American Mineralogist, published by the Mineralogical Society of America.
The published version is subject to change. Cite as Authors (Year) Title. American Mineralogist, in press.
DOI: https://doi.org/10.2138/am-2022-8289. http://www.minsocam.org/

Figure 7. F mineral/melt partition coefficient against fluid composition in the olivine lamproite series. The effect of water activity is most noticeable in the 1050°C series, with high partition coefficients associated with water-poor (methane-rich) fluids; the strong decreases result from increased water activity.

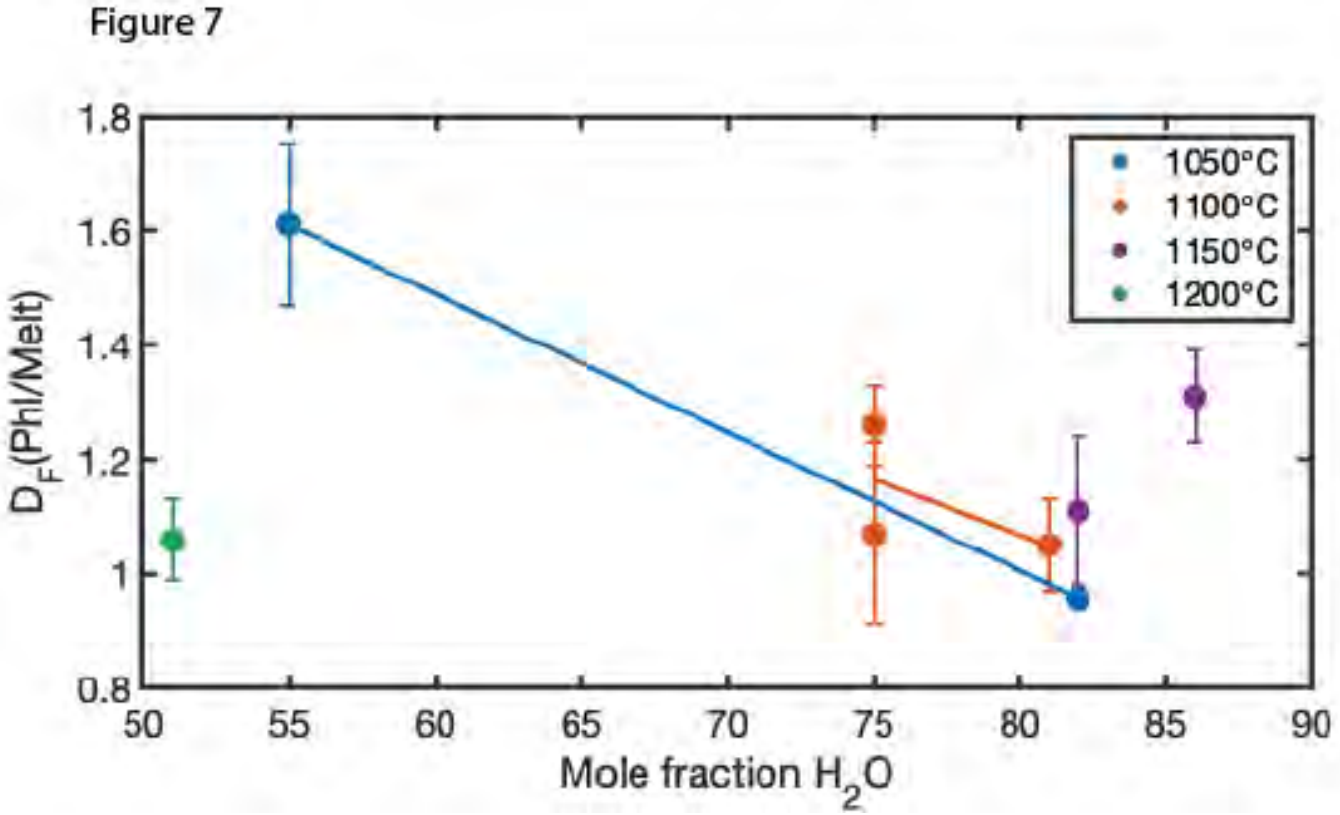

This is the peer-reviewed, final accepted version for American Mineralogist, published by the Mineralogical Society of America.
The published version is subject to change. Cite as Authors (Year) Title. American Mineralogist, in press.
DOI: https://doi.org/10.2138/am-2022-8289. http://www.minsocam.org/

Figure 8

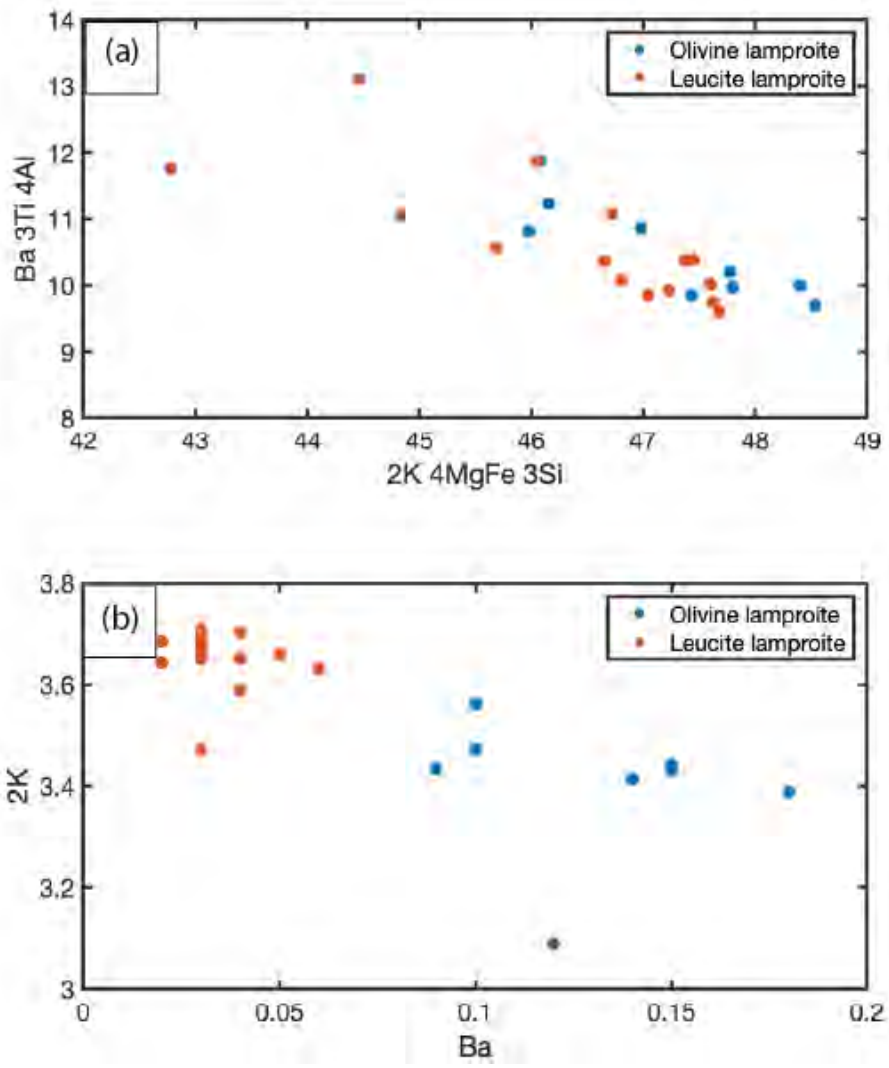

Figure 8. Substitution mechanisms for barium incorporation into phlogopite. (a) The substitution mechanism proposed by Guo and Green, (1990) $2K + 4(Mg, Fe) + 4Si = Ba + 3Ti + 4Al + [\,]_{VI.XII}$. (b) Simple substitution of $2K = Ba + [\,]$. Both substitution mechanisms appear to be operating in the experimental phlogopites. Underfilled octahedral and interlayer cation sites (see Table 3) favour the substitution mechanism in (a).

This is the peer-reviewed, final accepted version for American Mineralogist, published by the Mineralogical Society of America.
The published version is subject to change. Cite as Authors (Year) Title. American Mineralogist, in press.
DOI: https://doi.org/10.2138/am-2022-8289. http://www.minsocam.org/

Figure 9. Modelled partial melting of three mantle sources for lamproites: Phl - Lherz = phlogopite garnet lherzolite, Phl -Harz = phlogopite harzburgite, Phl - Pyrox = hydrous phlogopite pyroxenite. Melt fraction (x) vs. F/H_2O ratios are presented here, with melt fractions at 1, 5, 10 and 15% for the modelled mantle sources. The purple background represents the range of F/H_2O ratios considered representative of natural lamproites: at melt fractions greater than 5% all three sources are able to reproduce F/H_2O ratios in the range of natural lamproites. For full details of the modelling parameters see discussion and supplementary table 1.

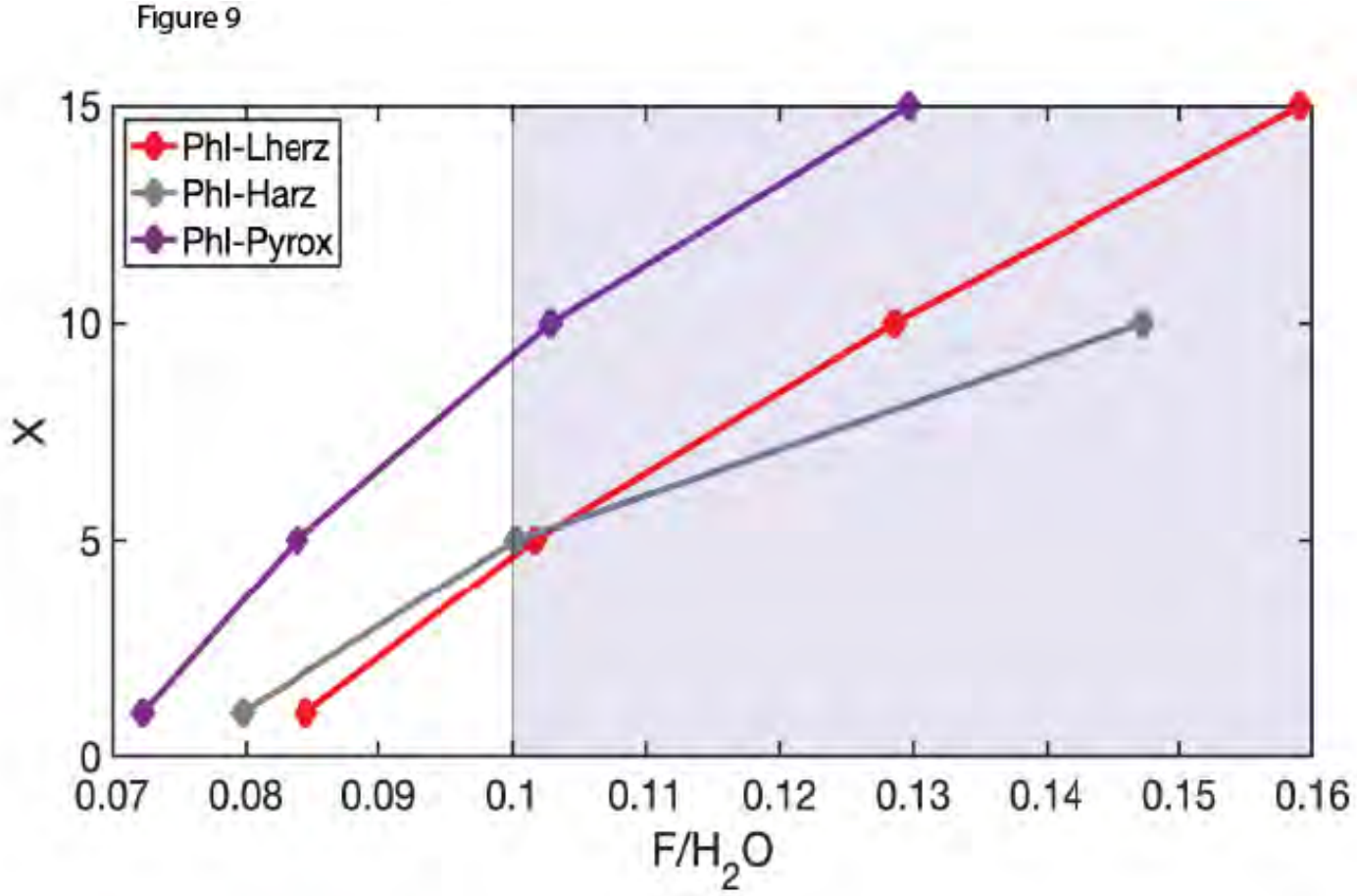

This is the peer-reviewed, final accepted version for American Mineralogist, published by the Mineralogical Society of America.
The published version is subject to change. Cite as Authors (Year) Title. American Mineralogist, in press.
DOI: https://doi.org/10.2138/am-2022-8289. http://www.minsocam.org/

Figure 10. Partial melting model for F/H_2O vs. F content, with the purple background representing the compositional range of natural lamproites. Mantle sources as described in Figure 7. Phl - harzburgite sources produce melts too enriched in F to be representative of lamproites, following exhaustion of phlogopite. Phlogopite garnet lherzolite and hydrous pyroxenites fall within the range expected for natural lamproites at small melt fractions.